

On type 1 active galactic nuclei with double-peaked [O III]. I. data sample and basic results

QI ZHENG,¹ YANSONG MA,¹ XUEGUANG ZHANG*,² QIRONG YUAN*,¹ AND WEIHAI BIAN¹

¹School of Physics and Technology, Nanjing Normal University, No. 1, Wenyuan Road, Nanjing, 210023, P. R. China

²Guangxi Key Laboratory for Relativistic Astrophysics, School of Physical Science and Technology, GuangXi University, No. 100, Daxue Road, Nanning, 530004, P. R. China

Submitted to ApJS

ABSTRACT

Double-peaked narrow emission lines (DPNELs) might be evidence for the existence of kpc-scale dual AGNs. There are so far large samples of objects with DPNELs in narrow emission line galaxies. Here, a systematic search is made to build a sample of type 1 AGNs with double-peaked [O III] from Data Release 16 of the Sloan Digital Sky Survey (SDSS). Through visually inspecting and fitting [O III], fitting broad H α emission lines, performing F-test for [O III] profiles, and checking broad H β and [O III] emission lines, we select 62 type 1 AGNs with reliable double-peaked [O III] from 11557 QSOs with $z < 0.3$. After visually checking the 62 SDSS multi-color images, we find only seven objects with signs of merging. Four possible models for the double-peaked [O III] observed in our sample are discussed: the superposition model, AGN outflow model, dual AGN model, and rotating disk model. However, the current results can not provide any one explanation conclusively, and additional observational data are needed to provide the details of narrow line regions. But at least 22 objects with different velocity offsets between double-peaked [O III] and narrow H α emission lines could be excluded as dual AGN candidates. The relative velocity offsets of the [O III] blue-shifted/red-shifted components are negative to their line flux ratios, which is consistent with dual AGN model. This work provides a new sample of 62 type 1 AGNs with double-peaked [O III] for further study.

Keywords: galaxies:active - galaxies:nuclei - galaxies:emission lines - galaxies:Seyfert

1. INTRODUCTION

It is widely accepted that central supermassive black holes (SMBHs) are present in most bulge-dominated galaxies (Kormendy & Richstone 1995; Kormendy & Ho 2013; Heckman & Best 2014). According to the hierarchical formation models, galaxy mergers frequently occur (Silk & Rees 1998; Mayer & Bonoli 2019; Zuo et al. 2022), and then facilitate the transportation of gas towards their central regions, initiate episodes of nuclear star formation, possibly trigger the activation of central supermassive black holes (Springel et al. 2005; Perna et al. 2023; Li et al. 2023). As a result, the force of dynamical friction comes into guiding each SMBH towards the center of the emerging mass distribution. This process can lead to the creation of a dual AGN with separations from kpc scale to pc scale (De Rosa et al. 2019). Subsequently, it progresses into a binary black hole (BBH) (Laine et al.

2020; Komossa et al. 2021) with sub-pc separation driven by gravitational wave emission, ultimately merging to form a larger SMBH. The studies on merging galaxies would provide valuable insights into the drivers of galaxy evolution, the estimation of the galaxy merger rate and the production of gravitational waves (Merritt & Milosavljević 2005; Komossa 2006; Arzoumanian et al. 2020). In this manuscript, we mainly focus on dual AGN systems around kpc-scale, and hereafter ‘dual AGN’ mentioned in the manuscript means system around kpc-scale.

While it is expected that dual AGN systems would be common in merger scenario, there are actually rare identified dual AGN systems as discussed in Bhattacharya et al. (2023). Considerable work has been put into seeking observational support for the existence of dual AGN systems through spatially resolved images in these years, such as in Komossa et al. (2003); Liu et al. (2011); Shen et al. (2019); Goulding et al. (2019); Zhang et al. (2021); Saturni et al. (2021); Bhattacharya et al. (2023); Zheng et al. (2023). For spatially resolved systems, dual AGN systems can be directly

Corresponding author: Xueguang Zhang; Qirong Yuan
 xgzheng@gxu.edu.cn; yuanqirong@njnu.edu.cn

identified by two bright cores as morphological characteristics.

However, due to the lack of spatial resolution, it is in most cases impossible to resolve the two nuclei. Therefore, some other spectroscopic features are applied to search for dual AGN systems, such as DPNELs (Xu & Komossa 2009) or shifted single-peaked narrow emission lines relative to absorption lines (Zheng et al. 2023). In this scenario, the orbital radial velocity of two nuclei is non-negligible, and it is spectroscopically observed as AGN emission lines produced by ionized gas. These emission lines exhibit velocity offsets relative to the stellar absorption lines. The latter are assumed to trace the systemic velocity of the host galaxy (Barrows et al. 2016). The main focus of the paper is the study of DPNELs related to kpc dual AGN systems.

The double-peaked narrow emission profiles are detected in both type 1 and type 2 AGNs and they are generally most prominent in [O III] $\lambda\lambda$ 4959, 5007. Zhou et al. (2004) found a type 2 quasar SDSS J1048+0055 with double-peaked profiles of [O III] $\lambda\lambda$ 4959, 5007 and two radio cores in 8.4 GHz, and first suggested that DPNELs might be an effective way to find dual AGN systems. Then there are several objects reported as dual AGN systems with both double-peaked profiles of [O III] and two cores in images as discussed in Comerford et al. (2011); McGurk et al. (2011); Liu et al. (2013); Woo et al. (2014), and several dual AGN candidates with DPNELs but no spatially resolved images as reported in Gerke et al. (2007); Barrows et al. (2012); An et al. (2013); Zheng et al. (2024). Moreover, besides the double-peaked profiles can be found in [O III], this features can also be found in the higher-ionization lines. Barrows et al. (2013) firstly reported the candidates of dual AGN systems at higher redshift with double-peaked [Ne V] λ 3426 or [Ne III] λ 3869 from the Sloan Digital Sky Survey (SDSS) Data Release 7 (DR7) to support dual AGN systems. Furthermore, as suggested by Xu & Komossa (2009), the presence of double-peaked profiles in all of its narrow emission lines, rather than just one, can be considered as a better proof to support exceptionally strong contenders for kpc-scale dual AGN systems. Up to the present, there are only SDSS J131642.90+175332.5 (Xu & Komossa 2009), SDSS J143132.84+435807.20 (Severgnini et al. 2021), and SDSS J222428.53+261423.2 (Zheng et al. 2024) reported such unambiguous double-peaked profiles in all optical narrow emission lines.

Unfortunately, it is difficult to confirm these objects with DPNELs as dual AGN systems because of lacking two spatially resolved cores. In addition to dual AGN systems, there are several alternative explanations for the double-peaked narrow emission profiles. The first alternative explanation for the DPNELs is the superposition of two extra-galactic emission line objects (superposition model). Xu & Komossa (2009) discussed this scenario in SDSS J131642.90+175332.5, and

Dotti & Ruszkowski (2010) investigated the peak separation between blue-shifted and red-shifted components (Δv) of a chance superposition. The second alternative explanation for the DPNELs is AGN outflow model. Several studies (Müller-Sánchez et al. 2015; Nevin et al. 2016; Comerford et al. 2018; Rubinur et al. 2019) suggested that the prevailing influence on objects with DPNELs is, indeed, outflows, and Nevin et al. (2016) claimed that this percentage can be as high as 86% from 71 type 2 AGNs at $z < 0.1$. The third alternative explanation for the DPNELs is rotating disk model. Smith et al. (2012) showed that it is likely that equal-peaked narrow emission profiles represent rotating disk.

Thus detecting double-peaked profiles in narrow emission lines alone is not sufficient to confirm objects as kpc-scale dual AGN systems. All these cases simply indicate the diverse nature of narrow line region (NLR) gas dynamics, so it is necessary for follow-up observations to confirm or refute kpc-scale dual AGN systems from the double-peaked [O III] sample. These follow-up observations include high-resolution imaging to detect spatially resolved cores. Fu et al. (2011a) published images of 50 AGNs ($z < 0.6$) with double-peaked [O III] from the Keck II laser guide star adaptive optics system (LGSAO; Wizinowich et al. 2006) and found that $\sim 30\%$ of the objects in their sample show discernible companions with a spatial resolution of $0.1''$. With the same instrument, Rosario et al. (2011) showed six objects with double galaxy structures and four objects in galaxy mergers from 12 QSOs ($0.2 < z < 0.6$) with double-peaked [O III]. Liu et al. (2013) examined and confirmed two dual AGNs from four candidates with double-peaked [O III] through the Hubble Space Telescope (HST) and Chandra imaging. By the same method, Comerford et al. (2015) confirmed a dual AGN with a 2.2 kpc separation in an extreme minor merger, which resulted in the double-peaked [O III] emission lines. While high-resolution imaging can detect two components with small separations, it can not confirm whether the double-peaked profiles are related to only one component.

In addition, spatially resolved spectroscopy is another method of follow-up observations besides high-resolution imaging. Long-slit spectroscopy is used to spectrally separate the DPNELs to determine whether the emission lines are from the regions along the slit. As discussed in Comerford et al. (2012), the double AGN emission components aligned with the host galaxy major axis are expected in case of dual AGN system orbiting in the host galaxy potential. Integral field spectroscopy offers high-quality and delicate spectra with smaller diameter apertures to support robust evidence of the origin of the double emission lines. As shown in Fu et al. (2012), integral-field spectroscopy resolves the kinematic components spatially, linking each to its respective core.

It is worth noting that many studies have combined imaging with spatially resolved spectroscopy to gain a more

comprehensive understanding of the sources with DPNELs. Comerford et al. (2009a) showed evidence for a dual AGN COSMOS J100043.15+020637.2, showing double-peaked [O III], with HST image ($1.75 \pm 0.03 h^{-1}$ kpc projected spatial offset) and slit spectroscopy. Liu et al. (2010b) reported four dual AGNs, whose locations of two cores in deep near-infrared images are coincident with those of two components of double-peaked [O III] in the slit spectra. McGurk et al. (2011) detected that SDSS J095207.62+255257.2 with double-peaked [O III] is confirmed as a dual AGN separated by 4.8 kpc, using LGSAO imaging and near-infrared integral-field spectroscopy. Fu et al. (2011b) confirmed SDSS J150243.09+111557.3 with double-peaked [O III] as a dual AGN separated by 7.4 kpc through the optical integral-field spectroscopy and high-resolution radio images. Shen et al. (2011a) reported that roughly 10% of 31 type 2 AGNs with double-peaked [O III] are dual AGNs and about 50% of them exhibit the kinematic signatures of a single NLR determined by both near infrared image and optical slit spectroscopy. Fu et al. (2012) discovered that only 2% of the double-peaked [O III] are produced by the orbital motion of the merging nuclei through combining integral-field spectroscopy with LGSAO imaging. A few years later, McGurk et al. (2015) claimed that 5% of double-peaked objects are dual AGNs through high-resolution imaging and spatially resolved integral field and long-slit spectroscopy.

Unfortunately, Villforth & Hamann (2015) showed that the combination of deep multi-band imaging and long-slit spectroscopy would sometimes fail to unambiguously identify the objects with double-peaked [O III] as dual AGNs. Moreover, the techniques mentioned above are suitable for identifying individual dual AGN systems with DPNELs, but quite expensive for discovering large samples of dual AGN system candidates by DPNELs. However, a larger sample of dual AGN system candidates with DPNELs is needed to understand the physical origins of DPNELs through statistical results. There are a growing number of objects with DPNELs through systematic searches in the SDSS (Wang et al. 2009; Smith et al. 2010; Liu et al. 2010a; Lyu & Liu 2016; Comerford et al. 2018; Maschmann et al. 2020; Kim et al. 2020b), the Large Sky Area Multi-Object Fiber Spectroscopic Telescope (Shi et al. 2014; Wang et al. 2019), and the DEEP2 Galaxy Redshift Survey (Comerford et al. 2009b). Maschmann et al. (2020) reported the largest sample to date of 5,663 galaxies displaying DPNELs, based on the Reference Catalogue of Spectral Energy Distribution (Chilingarian et al. 2017), to analyze host-galaxy properties and kinematics; however, this dataset remains non-public. In comparison, Ge et al. (2012) reported a publicly available sample of 3,030 DPNEL galaxies from SDSS DR7.

However, the majority of the reported objects with DPNELs are narrow emission line galaxies (type 2 AGNs, star-forming

galaxies, etc.). Combining with the narrow emission line galaxies with DPNELs, broad emission line galaxies with DPNELs will provide more clues to test and/or identify the physical origin of DPNELs. Therefore, we carry out a systematic search for type 1 AGNs with double-peaked [O III] from the SDSS DR16 (Ahumada et al. 2020).

The paper is organized as follows. In Section 2, we show our main procedure to collect the type 1 AGNs with double-peaked [O III] from the parent sample of quasars in SDSS DR16. In Section 3, basic physical parameters are measured for the collected type 1 AGNs with DPNELs. In Section 4, the possible explanations for the DPNELs in this paper are given. The main conclusions are given in Section 5. In this paper, we adopt the cosmological parameters of $H_0 = 70 \text{ km} \cdot \text{s}^{-1} \text{Mpc}^{-1}$, $\Omega_\Lambda = 0.7$ and $\Omega_m = 0.3$.

2. SAMPLE SELECTION

For the goal of selecting type 1 AGNs with double-peaked [O III], the objects classified as QSOs in Ross et al. (2012); Pâris et al. (2018); Lyke et al. (2020) (https://www.sdss4.org/dr16/algorithms/qso_catalog/) in SDSS DR16 (Ahumada et al. 2020) are mainly considered. The details are described below in six steps, and a corresponding brief flow chart of the whole procedure is shown in Figure 1.

In the first step, a parent sample of SDSS QSOs are created through the SDSS SQL tool by the following two criteria of spectroscopic results of $z < 0.3$ and signal-to-noise ratio (S/N) larger than 10. The criterion of $z < 0.3$ is applied to ensure H α totally covered in SDSS spectra. The criterion of S/N is applied for the reliable measurements of emission line parameters. Then the applied SQL query (<https://skyserver.sdss.org/dr16/en/tools/search/sql.aspx>) in detail is as follows:

```
SELECT s.ra, s.dec, s.z, s.snmedian
FROM specobjall as s
WHERE
s.class='qso' and s.z<0.3 and
s.zwarning=0 and s.snmedian>10
```

The database of SpecObjAll (<https://skyserver.sdss.org/dr16/en/help/brow>) contains all the basic spectroscopic information. As a result, the parent sample, containing 11557 QSOs from SDSS DR16, is obtained.

In the second step, the spectra around [O III] are visually inspected and simply fitted by Gaussian functions. The spectra of all the quasars in the parent sample are displayed on the screen with rest wavelength coverage from 4900 to 5050 Å, and five people independently inspect the spectra **by eyes**. Not only the objects with apparent double-peaked [O III] emission features but also the objects with plateau and strange emission features around [O III] are chosen as candidates with double-peaked [O III]. Here, the ‘double-peak’

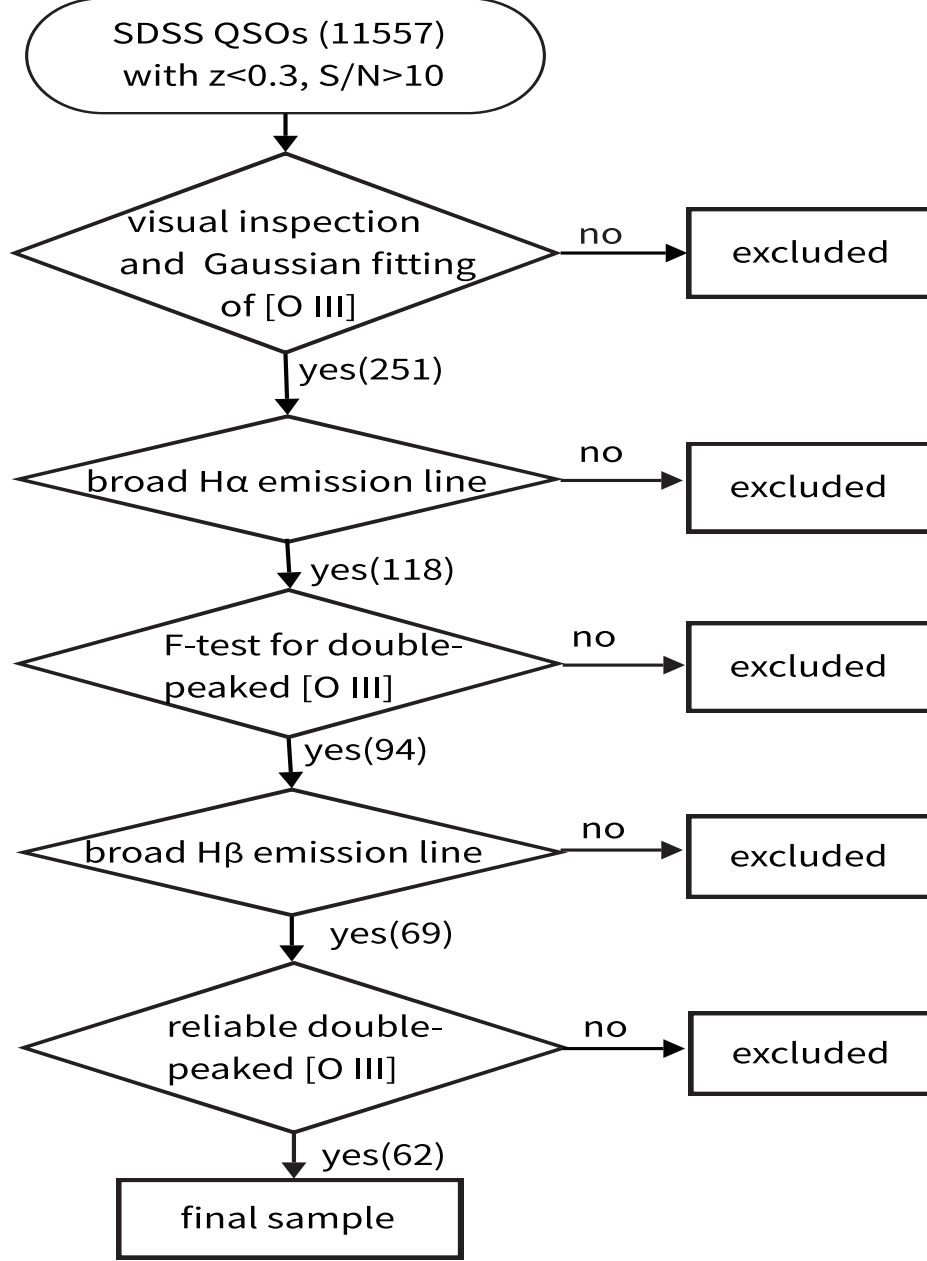


Figure 1. The flow chart in this work.

means the presence of two distinct peaks near $[O\ III]\lambda 5007$ separated by a dip, while ‘plateau’ indicates a single peak near $[O\ III]\lambda 5007$, with adjacent points maintaining values comparable to the maximum. One object would be eventually collected as a candidate, if it is thought to have double-peaked emission features of $[O\ III]$ by at least three people. Besides, $[O\ III]$ doublet is simply described by six narrow Gaussian functions (four Gaussian functions for the possible double-peaked profiles and two Gaussian functions for the extended components). If $[O\ III]$ doublet of one object can be fitted by six Gaussian functions or by four Gaussian functions (with very weak extended components), it is left as a candidate with

DPNELs. All the objects selected according to the two methods mentioned above are saved. The undeniable fact is that those methods might mistakenly identify $Fe\ II$ lines as peaks of $[O\ III]$ lines, but this is just a preliminary screening, and these objects will be further processed in detail afterwards. Among all the 11557 QSOs in parent sample, 251 objects are firstly selected as candidates of type 1 AGNs with probable double-peaked $[O\ III]$.

In the third step, the emission lines around $H\alpha$ are modeled, in order to reconfirm the collected objects as type 1 AGNs with broad $H\alpha$. Due to the apparent host galaxy contributions in some of the SDSS spectra of the

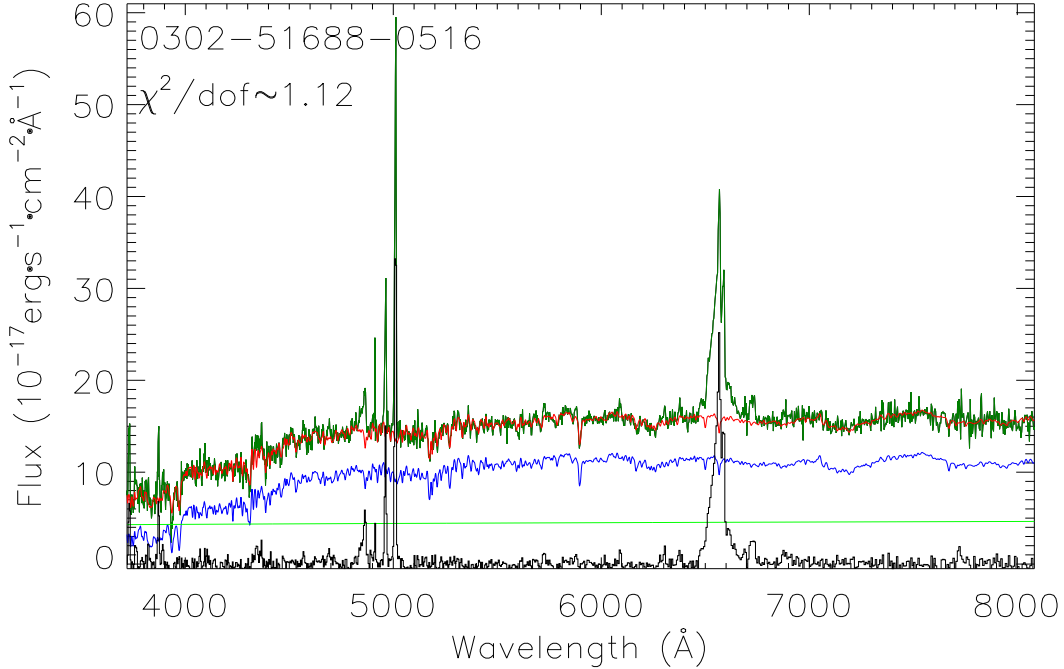


Figure 2. An example of SDSS spectrum in the final sample. The solid dark green line represents the spectrum with Plate-Mjd-Fiberid shown in the top-left of corner, the solid red line shows the best fitting results with χ^2/dof shown in the top-left of corner, the solid blue line shows starlight, the solid green line represents the AGN continuum emission, and the solid black line represents the line spectrum calculated by the SDSS spectrum minus the best fitting results.

collected 251 objects, the simple stellar population (SSP) method (Bruzual & Charlot 1993, 2003; Kauffmann et al. 2003; Cid Fernandes et al. 2005; Cappellari 2017) is firstly applied to describe the contributions of starlight. The same method can be found in Zhang (2014, 2021a, 2024a,b). Host galaxy contribution can be modeled by combination of the 39 broadened, strengthened and shifted SSPs with 13 population ages ranging from 5 Myr to 12 Gyr and 3 metallicities ($Z=0.008, 0.05, 0.02$) as described and discussed in Kauffmann et al. (2003); Bruzual & Charlot (2003). Meanwhile, a power law function is applied to describe AGN continuum emission. Then through the Levenberg-Marquardt least-squares minimization technique (the MPFIT package; Markwardt 2009), the observed spectrum of the object with apparent host galaxy contribution can be described by SSPs plus a power law function. In addition, when the SSP method is applied, the emission lines are masked out with FWZI (Full Width at Zero Intensity) about 400 km/s, and broad Blamer lines and possible Fe II emission lines are masked out with rest wavelength from 4400 to 5600 Å and from 6400 to 6700 Å. Here, we do not show the best fitting results of all the firstly collected 251 objects, but Figure 2 shows an example, SDSS J141003.66+001250.2 (Plate-Mjd-Fiberid: 0302-51688-0516), as one of the targets in our final sample of 62 type 1 AGNs with double-peaked [O III]. And the best fitting results to all the 62 targets are shown in the Figure 12 in the Appendix A. As shown in Figure 2 and Figure 12, 26 objects

do not show host galaxy contributions due to the very stronger AGN emission features. It is worth noting that there is an object (Plate-Mjd-Fiberid: 2652-54508-0025) with very weak AGN continuum emission but confirmed with both broad H α and H β emission lines in the later.

After subtracting the host galaxy contributions, the emission lines around H α (rest wavelength from 6200 to 6880 Å) can be modeled as follows. A narrow plus two broad Gaussian functions (second moment σ smaller or larger than 600 km/s) are applied to describe the H α emission line. Each of [SII] ([OI], [NII]) doublet is described by a Gaussian function, and the Gaussian components of doublet have the same redshift and line width in velocity space. Meanwhile, the flux ratio of [NII] doublet is set as the theoretical flux ratio 3. A power law component is applied to describe possible continuum emission underneath the emission lines around H α . Based on the Levenberg-Marquardt least-squares minimization technique, the emission lines around H α can be determined. Then, among the firstly collected 251 objects, 118 objects with reliable broad H α emission lines are selected through the following criteria:

$$\sigma > 13\text{\AA} (\sim 600 \text{ km/s}), \frac{\sigma}{\sigma_{\text{error}}} > 3, \frac{f}{f_{\text{error}}} > 3, \quad (1)$$

where σ and σ_{error} (in units of Å) are the second moment and the corresponding uncertainty determined by MPFIT of one of the Gaussian components applied to describe broad

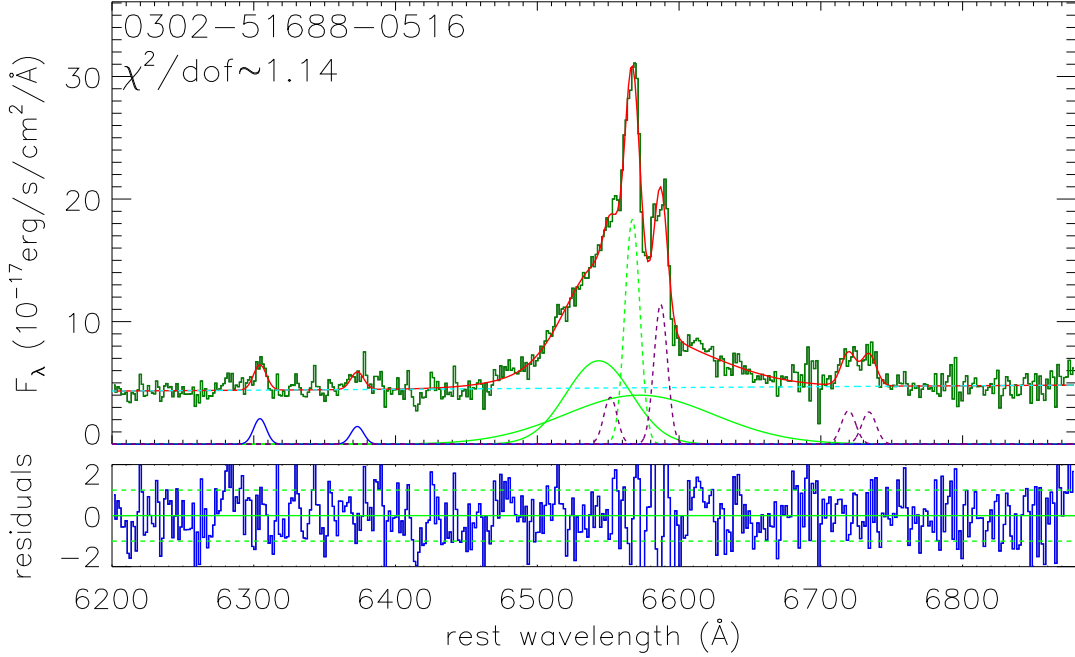


Figure 3. An example of the best fitting results of the emission lines around H α . In the top panel, the solid dark green line shows the line spectrum after subtracting starlight from host galaxy with Plate-Mjd-Fiberid shown in the top-left of corner, the solid red line represents the best fitting results with χ^2/dof shown in the top-left of corner, the dashed cyan line represents continuum emission, the solid green lines represent the determined components of broad H α emission line, the dashed green line represents narrow H α emission line, the solid blue lines represent [O I] emission lines, and the dashed purple lines represent [N II] and [S II] doublets. In the bottom panel, the solid blue line represents the residuals calculated by the line spectrum minus the best fitting results and then divided by uncertainties of SDSS spectrum, the horizontal solid and dashed green lines show residuals=0, ± 1 , respectively.

H α , and f and f_{error} (in units of $10^{-17} \text{erg/s/cm}^2$) are the flux and the corresponding uncertainty of emission components of broad H α . The other 133 objects are rejected since there are no reliable broad H α emission lines. According to the fitting results, the redshift relative to the central wavelength of narrow H α emission line is consistent to that of [N II], which supports the reasonable measurements of narrow lines, even there are weak [N II]. Figure 3 (complete results for all 62 objects shown in Figure 13 in Appendix A) shows the best fitting results of the emission lines around H α of the final 62 type 1 AGNs with double-peaked [O III]. Among Figure 3 and Figure 13 in Appendix A, one point should be noted. There are very broad components around 6730 Å in some objects (Plate-Mjd-Fiberid: 11040-58456-0394, 11347-58440-0066, 1403-53227-0485, 1944-53385-0120 and 7283-57063-0660) and it is hard to accurately describe the [S II] doublet.

In the fourth step, the emission lines around H β (rest wavelength from 4400 to 5600 Å), including probable optical Fe II emission features, are modeled and the F-test technique (Makridakis et al. 1997; Ge et al. 2012) is applied to check whether there are reliable double-peaked profiles of [O III]. Considering probable double-peaked emission features, two narrow Gaussian functions for the core component, and a broad Gaussian function ($\sigma > 400$ km/s) for the extended component (Greene & Ho 2005a; Shen et al. 2011b; Zhang

2021b) are applied to describe each of [O III] doublet. Meanwhile, corresponding Gaussian components of [O III] doublet have the same redshift and line width in velocity space, and the flux ratio set to 3. And a power law component is applied to describe AGN continuum emission. A broad Gaussian function is applied to describe He II emission line. The optical Fe II emission templates in the four groups discussed in Kovacevic et al. (2010) are applied to describe the optical Fe II features. Two broad Gaussian functions ($\sigma > 600$ km/s) are applied to describe the profile of broad H β emission line. A narrow Gaussian function is applied to describe narrow H β emission line since the following two reasons. First, we mainly focus on the double-peaked profiles of [O III]. Second, the H β emission line is rather weak, which will not affect the reliability of broad H β discussed in the next step. Moreover, we also try to fix the central wavelengths of narrow H β and H α with these of double-peaked [O III] to describe possible double-peaked narrow H β and H α emission lines, but could not find appropriate results. Only nine objects show clear double-peaked narrow H α emission lines as shown afterwards.

It is known that there are apparent emission features of the optical Fe II around [O III], leading to effects on detecting double-peaked [O III]. Therefore, the emission lines around H β and [O III] are described by model functions, with the rest

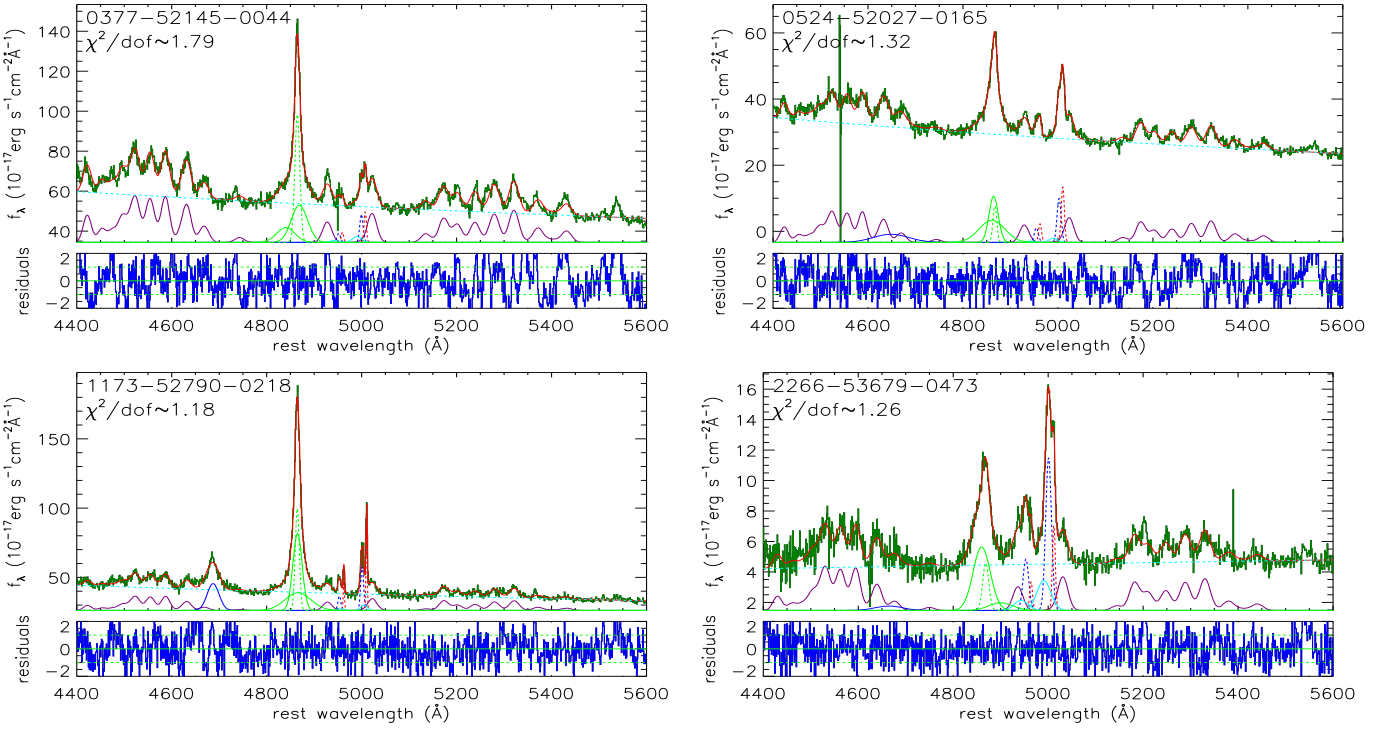


Figure 4. Four examples on the best fitting results of FeII emission lines. In the top of each panel, the solid dark green line shows the line spectrum after subtracting starlight (if present) determined from host galaxy with Plate-Mjd-Fiberid shown in the top-left of corner, the solid red line represents the best fitting results with χ^2/dof shown in the top-left of corner, the solid blue line represents He II emission line (if present), the solid purple lines represent Fe II emission lines, and the dashed cyan line represents continuum emission, the solid green lines represent broad H β emission line, the dashed green line represents narrow H β emission line, the solid cyan lines represent extended components of [O III], and the dashed blue and red lines represent the blue-shifted and red-shifted components of [O III], respectively. In the bottom of each panel, the solid blue line represents the residuals calculated by the line spectrum minus the best fitting results and then divided by uncertainties of SDSS spectrum, the horizontal solid and dashed green lines show residuals=0, ± 1 , respectively.

Table 1. sample information

Plate-Mjd-Fiberid (1)	RA (2)	DEC (3)	z (4)	mag _r (5)	S/N (6)	FIRST (7)	R (8)	Reference (9)
0302-51688-0516	212.51527	0.21395	0.14	18.4 ± 0.01	15.19	0	0	-
0307-51663-0219	219.25504	-1.07168	0.29	19.03 ± 0.08	11.15	0	0	-
0332-52367-0639	184.03066	-2.23828	0.1	17.28 ± 0.01	29.36	0	0	(1),(2)
0377-52145-0044	340.12026	-1.11381	0.13	17.25 ± 0.02	27.98	0	0	-
0394-51913-0111	13.6107	-0.339	0.17	19.03 ± 0.01	25.54	10.53	237.98	-
0448-51900-0084	133.73845	54.80571	0.26	18.2 ± 0.02	15.73	1.31	11.78	-
0452-51911-0080	145.43677	57.85658	0.16	17.97 ± 0.01	15.12	0	0	(1),(2),(6),(7)
0524-52027-0165	196.07083	2.09365	0.23	17.33 ± 0.02	25.71	0	0	-
0555-52266-0033	144.88269	54.81924	0.29	18.31 ± 0.01	15.56	0	0	-
0609-52339-0435	221.95334	62.74577	0.23	18.49 ± 0.02	11.75	0	0	(1),(2),(8)

Notes. Column 1: Plate, MJD, Fiberid of spectroscopic observation; Column 2: RA; Column 3: DEC; Column 4: Redshift of spectroscopic observation; Column 5: Apparent psf magnitude in r band; Column 6: Median signal-to-noise over all good pixels; Column 7: Integrated FIRST radio flux(mJy); Column 8: Radio-loudness; Column 9: Reference:(1) Zhang & Feng (2016); (2) Smith et al. (2010); (3) Ge et al. (2012); (4)Smith et al. (2012); (5) Zheng et al. (2024); (6) Fu et al. (2012); (7) Comerford et al. (2018); (8) Kim et al. (2020b); (9) Comerford et al. (2012); (10) McGurk et al. (2015); (11) Rosario et al. (2011); (12) Fu et al. (2011a).

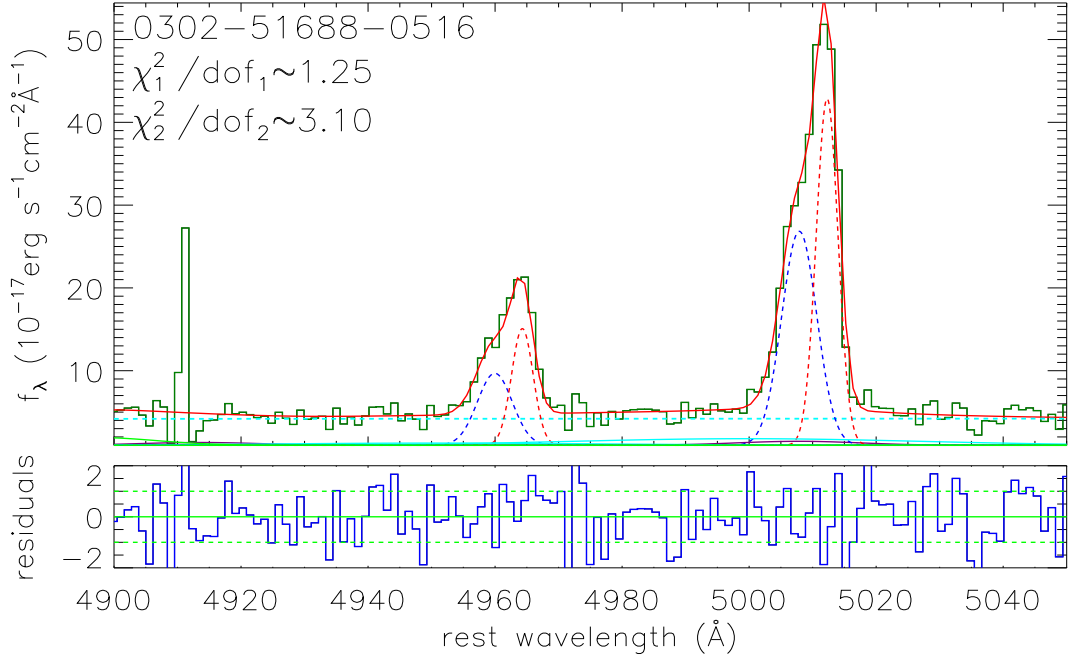


Figure 5. An example of the best fitting results of the emission lines around [O III]. In the top panel, the solid dark green line shows the line spectrum after subtracting starlight determined from host galaxy with Plate-Mjd-Fiberid shown in the top-left of corner, the solid red line represents the best fitting results with two narrow Gaussian functions describing each core component of [O III] doublet, and the corresponding χ^2/dof_1 is shown in the top-left of corner, the χ^2/dof_2 determined by one narrow Gaussian function for each core component of [O III] doublet is shown in the top-left of corner, the dashed cyan line represents continuum emission, the solid purple lines represent Fe II emission lines, the solid green lines represent broad H β emission line, the solid cyan lines represent extended component of [O III], and the dashed blue and red lines represent the blue-shifted and the red-shifted components of [O III], respectively. In the bottom panel, the solid blue line represents the residuals calculated by the line spectrum minus the best fitting results and then divided by the uncertainties of the SDSS spectrum, the horizontal solid and dashed green lines show residuals=0, ± 1 , respectively.

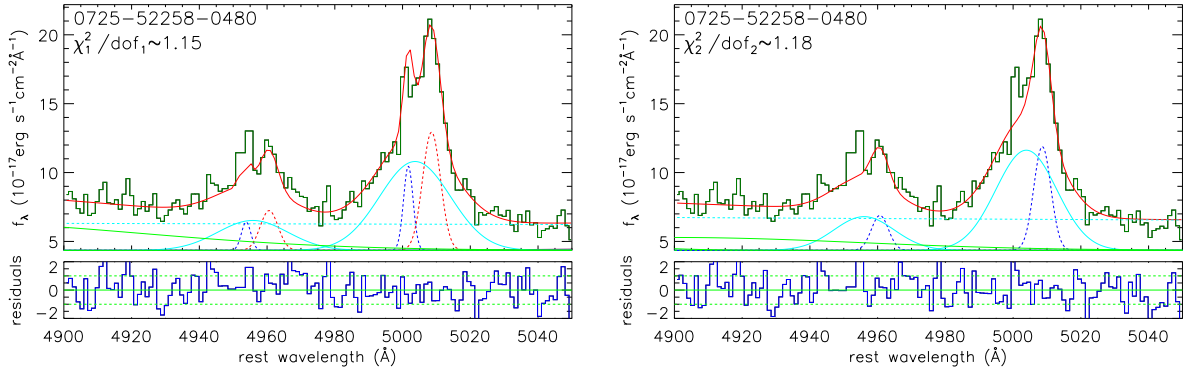


Figure 6. An example of type 1 AGN excluded by F-test. In the top of each panel, the solid dark green line shows the line spectrum after subtracting starlight determined from host galaxy with Plate-Mjd-Fiberid shown in the top-left of corner, the solid red line represents the best fitting results with χ^2/dof_1 (χ^2/dof_2) of two (one) narrow Gaussian functions for each core component of [O III] doublet, the dashed cyan line represents continuum emission, the solid green lines represent broad H β emission line, the solid cyan lines represent extended [O III] components. The dashed blue and red lines (in the top-left panel) represent the blue-shifted and red-shifted components of [O III], respectively. The dashed blue line (in the top-right panel) represents the single peak of [O III]. In the bottom of each panel, the solid blue line represents the residuals calculated by the line spectrum minus the best fitting results and then divided by uncertainties of SDSS spectrum, the horizontal solid and dashed green lines show residuals=0, ± 1 , respectively.

wavelength from 4400 to 5600 Å to totally cover optical Fe II. Figure 4 shows several objects with strong Fe II. It seems that the apparent peaks around [O III] are actually produced by optical Fe II, which could potentially be misidentified as double-peaked [O III], especially in the top-left panel of Figure 4.

Due to the main focus on double-peaked [O III], the best fitting results around [O III] doublet (rest wavelength from 4900 to 5050 Å) with two narrow plus one broad Gaussian functions for each of the [O III] doublet, referred as ‘model 1’, are shown in Figure 5 (complete results for all 62 objects shown in Figure 14 in Appendix A). The corresponding χ^2_1 in Figure 5 is re-calculated related to the best fitting results with the rest wavelength from 4900 to 5050 Å, and the dof₁ (degrees of freedom) is determined by numbers of data points minus eleven (nine in the three Gaussian functions for [O III] λ 5007 and two in the power law component underneath the [O III] doublet). Here, the value of dof₁ for the model 1 does not consider the number of model parameters for the optical Fe II, because the same optical Fe II, treated as a constant component, determined by the best fitting results with rest wavelength from 4400 to 5600 Å are considered both in the model 1 and the following model 2. So there is a little difference of shown χ^2/dof between Figure 4 and 5.

Large wavelength range is not appropriate to do the following F-test, therefore, the range between 4900 to 5050 Å is considered. In order to test reliability of the double-peaked [O III] through the F-test technique, another model, referred as ‘model 2’, is applied to describe the [O III] emission lines. In the model 2, there is only a narrow plus a broad Gaussian functions applied to describe each of the [O III] doublet. There is also a power law component applied to describe possible continuum emission. Then, the same restrictions used in model 1 are applied in model 2 in [O III] doublet. Through the same MPFIT package, the best fitting results with χ^2_2/dof_2 can be determined to the [O III] doublet. Based on the different χ^2/dof values for the model 1 and the model 2 for the [O III] emissions line fittings, the calculated F_p (Makridakis et al. 1997; Ge et al. 2012) value can be described as

$$F_p = \frac{\frac{\chi^2_2 - \chi^2_1}{\text{dof}_2 - \text{dof}_1}}{\chi^2_1 / \text{dof}_1}. \quad (2)$$

According to $\text{dof}_2 - \text{dof}_1 = 3$ and dof_1 as number of dofs of the F distribution numerator and denominator, the expected value from the statistical F-test with confidence level about 3σ will be near to F_p value of 4.99. For the spectra with wavelength ranging from 4900 to 5050 Å, the numbers of data are all about 131 ($\text{dof}_1 = 120$ and $\text{dof}_2 = 123$). Here, the 94 AGNs with confidence level higher than 3σ are preferred to have double-peaked [O III], rather than single-peaked [O III]. For example, the AGN (Plate-Mjd-Fiberid: 7875-56980-0296) is preferred to have DPNELs due to $\chi^2_1 = 109$, $\chi^2_2 = 1004$ with

confidence level higher than 5σ ($F_p=328$). Figure 6 shows an example excluded by F-test with confidence level less than 3σ ($F_p=2$) with $\chi^2_1 = 138$ and $\chi^2_2 = 145$.

In the fifth step, the modeled parameters of H β emission lines are checked to identify true type 1 AGNs with broad H β emission lines. Similar criteria as described in equation (1) are applied here. Then, 69 type 1 AGNs in our work are retained.

In the sixth step, we refine our selection process by identifying more reliable candidates for the final sample based on the following criterion. We select 62 type 1 AGNs into the final sample with second moment and line flux of double-peaked [O III] three times larger than their uncertainties. The 62 type 1 AGNs in our work with reliable double-peaked [O III] are confirmed as true type 1 AGNs with both broad H β and H α emission lines. Basic information of the 62 AGNs in the final sample is listed in Table 1 including Plate-Mjd-Fiberid, RA, DEC, redshift, photometric magnitude in r -band, S/N. Since the broad H β components are applied only to verify true type 1 AGNs, the parameters of the central wavelength, line width and flux of broad H β emission lines determined from line profiles of two broad Gaussian functions are listed in Table 2. Similarly, parameters of broad H α emission lines are listed in Table 2. The features of [N II] and narrow H α emission lines are listed in Table 3. Meanwhile, the modeled parameters of double-peaked [O III] and the results of F-test are shown in Table 4. For clarity, here, we present the information of several AGNs of the final sample in the main text of the manuscript; the corresponding full information of all 62 type 1 AGNs is provided in Appendix B.

3. BASIC PROPERTIES OF TYPE 1 AGNS WITH DPNELS

In this section, basic properties of the 62 type 1 AGNs with DPNELs in this work are measured and discussed.

3.1. Black hole mass

Based on the virialization assumption to emission clouds in broad line regions (BLRs) (Peterson et al. 2004; Greene & Ho 2005b; Shen et al. 2011b; Rafiee & Hall 2011), the virial black hole mass (Greene & Ho 2005b; Ananna et al. 2022) in this work can be determined in the 62 type 1 AGNs with double-peaked [O III] by incorporating the established correlation between broad line region size (estimated via reverberation mapping) and continuum luminosity (Bentz et al. 2013). The equation (Peterson et al. 2004; Greene & Ho 2005b; Mejía-Restrepo et al. 2022) can be described as:

$$M_{\text{BH}} = 2.67 \times 10^6 \left(\frac{L_{\text{H}\alpha}}{10^{42} \text{ erg/s}} \right)^{0.55} \times \left(\frac{\text{FWHM}_{\text{H}\alpha}}{10^3 \text{ km/s}} \right)^{2.06} M_{\odot}, \quad (3)$$

Here, the equation is used due to consideration of the best match H β -related (RM) measurements. In this equation, FWHM $_{\text{H}\alpha}$ is the full width at half maximum, and L $_{\text{H}\alpha}$ is the luminosity of broad H α emission line after considering interstellar extinction given by Fitzpatrick (1999) with assumption of the intrinsic Balmer decrement 3.1 for broad H α to broad H β . The mean value of the estimated black hole masses for the 62 type 1 AGNs is about logM $_{\text{BH}}/M_{\odot} \sim 7.96 \pm 0.05$, and the uncertainty is determined by the uncertainties of FWHM $_{\text{H}\alpha}$ and L $_{\text{H}\alpha}$. Meanwhile, the estimated black hole masses are listed in Table 2 (complete results for all 62 objects shown in Table 7 in Appendix B).

Then, it is possible to examine whether the black hole masses of our sample are different from black hole masses of normal type 1 AGNs with single-peaked narrow emission lines. Here, a sample of normal type 1 AGNs is constructed from the Shen et al. (2011b) dataset, which includes 105,783 QSOs from SDSS DR7. To minimize the influence of differing evolutionary histories, a new sample of 558 normal type 1 AGNs with single-peaked [O III] $\lambda 5007\text{\AA}$ is randomly selected from the Shen et al. (2011b) dataset, ensuring a redshift distribution similar to that of our sample. According to a Kolmogorov–Smirnov (K-S) test (Kolmogorov 1933; Smirnov 1948), the redshift distributions of our sample and the newly constructed sample of 558 AGNs are statistically similar, with a probability of 99.99%. The redshift distributions are displayed in the left panel of Figure 7.

Here, in order to ignore effects of the different equations applied on virial BH masses, the M_{BH} of the 558 objects is calculated by the same way based on equation (3) with the parameters of broad H α emission lines from Table 1

in Shen et al. (2011b), and the mean value is $\log M_{\text{BH}}/M_{\odot} \sim 8.01 \pm 0.06$. Meanwhile, the distributions of the black hole masses M_{BH} of the 62 type 1 AGNs with double-peaked [O III] in our sample and the 558 typical type 1 AGNs are shown in the right panel of Figure 7. Then, the Student's t-test technique (Student 1908) is applied to check whether the 62 type 1 AGNs with DPNELs and the normal type 1 AGNs have significantly different mean values of virial black hole masses. The 62 type 1 AGNs show the same mean value of M_{BH} with the 558 typical type 1 AGNs with the probability of 47.86%.

3.2. Radio-loudness

The radio-loudness R is a classical tool to indicate the power of AGN outflows related to the accretion flow (Kellermann et al. 1989; Giarratana et al. 2023; Kynoch et al. 2023), and the R can be defined as $R = \nu_{5\text{GHz}} L_{5\text{GHz}} / \nu_{opt} L_{opt}$ (Sikora et al. 2007), where L_{opt} represents the luminosity at 5100 \AA after subtracting starlight (if present) and $L_{5\text{GHz}}$ is the luminosity at 5GHz determined by the integrated flux from the Faint Images of the Radio Sky at Twenty cm (FIRST) (Becker et al. 1995; White et al. 1997; Helfand et al. 2015), and $\nu_{5\text{GHz}}$ and ν_{opt} are their corresponding frequencies. The radio fluxes can be obtained through SQL query as follows:

```
SELECT s.ra, s.dec, s.z, s.snmedian,
F.integr
FROM specobjall AS s
JOIN FIRST AS F
ON F.objID=s.bestobjid
WHERE
class='qso' and s.z<0.3 and s.zwarning=0
and s.snmedian>10
```

The SDSS provided public database of FIRST (<https://skyserver.sdss.org/dr16/en/help/browser/browser.aspx?cmd=desc>) contains matched parameters of SDSS objects that match to FIRST objects. The collected integrated radio fluxes are listed in Table 1 (complete results for all 62 objects shown in Table 6 in Appendix B).

There are 9 type 1 AGNs outside the footprint of the FIRST survey, 34 type 1 AGNs below the detection limit (radio flux as zero) and 19 type 1 AGNs with radio fluxes beyond zero in our final sample. For our final sample, the fraction of type 1 AGNs with radio fluxes in the FIRST footprint is 35% (19/53), whereas this fraction is 16% in our parent sample. Typically, an object is classified as radio-loud if $R > 10$ (Kellermann et al. 1989). In total, there are 11 radio loud AGNs in our sample and the results of R are listed in Table 1 (complete results for all 62 objects shown in Table 6 in Appendix B). However, the 34 type 1 AGNs in our sample with radio fluxes reported as zero do not necessarily lack radio fluxes. Some of these AGNs may have radio fluxes that fall below the FIRST detection limit, potentially due to the orientation of their outflows (Smith et al. 2010). In our final sample, the fraction of radio-loud type 1 AGNs in the

Table 2. Line parameters of broad H α and broad H β

Plate-Mjd-Fiberid (1)	$\lambda_{H\alpha}$ (2)	FWHM $_{H\alpha}$ (3)	$F_{H\alpha}$ (4)	$\lambda_{H\beta}$ (5)	FWHM $_{H\beta}$ (6)	$F_{H\beta}$ (7)	mass (8)
0302-51688-0516	6559.7 ± 5.0	72.3 ± 5.7	918.7 ± 116.2	4850.9 ± 3.1	35.9 ± 5.4	96.4 ± 17.7	7.81 ± 0.10
0307-51663-0219	6569.2 ± 0.6	47.7 ± 5.0	881.3 ± 55.5	4864.9 ± 0.8	43.7 ± 2.6	188.6 ± 9.3	7.50 ± 0.11
0332-52367-0639	6565.3 ± 1.6	99.4 ± 3.9	3770.8 ± 226.9	4870.1 ± 2.1	102.5 ± 5.9	768.8 ± 50.6	7.98 ± 0.05
0377-52145-0044	6546.1 ± 0.5	73.3 ± 5.4	4751.0 ± 153.0	4859.9 ± 1.6	50.8 ± 2.8	1154.8 ± 66.7	7.80 ± 0.07
0394-51913-0111	6566.3 ± 1.7	35.2 ± 4.0	1141.8 ± 94.9	4863.3 ± 1.9	23.2 ± 4.6	46.0 ± 10.5	7.77 ± 0.12
0448-51900-0084	6567.9 ± 0.3	40.8 ± 4.5	1700.1 ± 58.8	4865.3 ± 1.7	35.2 ± 5.9	544.7 ± 28.4	7.28 ± 0.11
0452-51911-0080	6555.0 ± 0.8	48.8 ± 2.1	2213.3 ± 33.9	4857.4 ± 4.3	130.1 ± 12.4	369.4 ± 31.6	7.59 ± 0.04
0524-52027-0165	6557.9 ± 0.6	48.8 ± 3.0	2387.4 ± 110.1	4857.4 ± 4.3	29.3 ± 12.4	369.4 ± 31.6	7.79 ± 0.07
0555-52266-0033	6566.7 ± 0.7	113.3 ± 1.3	2854.9 ± 66.8	4869.4 ± 16.5	87.2 ± 33.1	824.1 ± 64.6	8.44 ± 0.02
0609-52339-0435	6561.2 ± 0.8	76.5 ± 1.7	1051.7 ± 30.6	4878.4 ± 15.8	51.3 ± 35.6	541.9 ± 72.0	7.69 ± 0.03

Notes. Column 1: Plate, MJD, Fiberid of spectroscopic observation; Column 2 and Column 3: the central wavelength (the first moment) of board H α in units of Å and corresponding FWHM of broad H α in units of Å determined through the line profiles described by two Gaussian functions, respectively; Column 4: corresponding flux of broad H α in units of 10^{-17} erg/s/cm 2 determined by the line flux described by two Gaussian functions; Column 5 and Column 6: the central wavelength (the first moment) of board H β in units of Å and corresponding FWHM of broad H β in units of Å determined through the line profiles described by two Gaussian functions, respectively; Column 7: corresponding flux of broad H β in units of 10^{-17} erg/s/cm 2 determined by the line flux described by two Gaussian functions; Column 8: the virial black hole mass $\log(M_{\text{BH}}/M_{\odot})$.

Table 3. Features of narrow H α and [N II] emission lines

Plate-Mjd-Fiberid (1)	$\lambda_{H\alpha}$ (2)	$\sigma_{H\alpha}$ (3)	$F_{H\alpha}$ (4)	$\lambda_{[\text{N II}]}$ (5)	$\sigma_{[\text{N II}]}$ (6)	$F_{[\text{N II}]}$ (7)
0302-51688-0516	6567.1 ± 0.2	5.3 ± 0.3	244.6 ± 23.8	6587.0 ± 0.2	4.7 ± 0.3	135.8 ± 14.0
0307-51663-0219	6569.1 ± 0.2	2.3 ± 0.2	77.4 ± 7.8	6589.3 ± 0.3	3.2 ± 0.3	70.7 ± 8.8
0332-52367-0639	6563.3 ± 0.2	4.3 ± 0.3	254.6 ± 25.8	6583.9 ± 0.2	4.2 ± 0.3	289.2 ± 26.5
0377-52145-0044	6567.8 ± 0.1	7.2 ± 0.1	3502.1 ± 55.5	6586.1 ± 0.3	4.9 ± 0.3	409.6 ± 38.0
0394-51913-0111	6559.6 ± 0.1	2.3 ± 0.1	125.7 ± 5.2	6585.2 ± 0.1	6.9 ± 0.2	471.1 ± 28.3
0448-51900-0084	6566.7 ± 0.1	2.2 ± 0.2	113.0 ± 8.9	6587.7 ± 0.2	4.2 ± 0.2	235.3 ± 13.6
0452-51911-0080	6564.0 ± 0.2	4.7 ± 0.2	339.4 ± 13.2	6585.0 ± 0.2	4.6 ± 0.2	281.5 ± 11.4
0524-52027-0165	6569.8 ± 0.1	7.1 ± 0.2	1176.8 ± 54.4	6592.7 ± 0.2	2.9 ± 0.2	107.9 ± 11.4
0555-52266-0033	6563.8 ± 0.4	6.5 ± 0.2	401.0 ± 19.8	6580.6 ± 1.0	8.0 ± 0.9	190.7 ± 35.3
0609-52339-0435	6567.5 ± 0.1	5.0 ± 0.1	600.3 ± 13.8	6586.4 ± 0.1	4.7 ± 0.2	276.5 ± 12.0

Notes. Column 1: Plate, MJD, Fiberid of spectroscopic observation; Column 2: the central wavelength of narrow H α in units of Å; Column 3: corresponding second moment of narrow H α in units of Å; Column 4: corresponding flux of narrow H α in units of 10^{-17} erg/s/cm 2 ; Column

5: the central wavelength of narrow [N II] in units of Å; Column 6: corresponding second moment of [N II] in units of Å; Column 7: corresponding flux of [N II] in units of 10^{-17} erg/s/cm 2 .

FIRST footprint is 20% (11/53). For comparison, the fraction of radio-loud AGNs is 23% in Barrows et al. (2013) sample, which shows double-peaked profiles in [Ne V] or [Ne III], and this fraction in their parent sample is 10%.

Both our sample and the Barrows et al. (2013) sample clearly indicate a preferential selection of radio objects among AGNs with DPNEs compared to the parent sample. This suggests that the origin of the double-peaked profiles in narrow emission lines may be associated with the presence of radio jets in some objects.

3.3. Photometric image properties

If the double-peaked [O III] emission lines were the results of dual AGN systems, it is expected for dual-cored galaxies or merging galaxies in the images. We visually inspect the SDSS images of the 62 type 1 AGNs in our sample and the SDSS multi-color images of seven visually interesting type 1 AGNs are shown in Figure 8.

SDSS J143701.20-010417.9 (Plate-Mjd-Fiberid: 0307-51663-0219) may be a major merger between two galaxies,

Table 4. Features of [O III]

Plate-Mjd-Fiberid (1)	λ_b (2)	σ_b (3)	F_b (4)	λ_r (5)	σ_r (6)	F_r (7)	F-test (8)	V_b (9)	V_r (10)
0302-51688-0516	5007.9 ± 0.5	2.8 ± 0.3	178.9 ± 29.6	5012.3 ± 0.1	1.7 ± 0.1	180.2 ± 28.4	5	173.2 ± 41.9	435.6 ± 19.4
0307-51663-0219	5001.0 ± 0.9	4.6 ± 0.6	78.2 ± 13.8	5009.4 ± 0.3	3.1 ± 0.2	87.3 ± 13.0	3	-	-
0332-52367-0639	5005.8 ± 0.1	1.9 ± 0.1	360.5 ± 16.0	5011.2 ± 0.2	1.8 ± 0.1	181.2 ± 15.6	5	112.5 ± 16.2	214.0 ± 19.8
0377-52145-0044	4999.5 ± 0.7	3.6 ± 0.7	121.2 ± 24.1	5007.5 ± 0.5	2.5 ± 0.4	94.5 ± 21.8	3	-	-
0394-51913-0111	5003.7 ± 0.1	1.8 ± 0.1	69.5 ± 7.0	5008.5 ± 0.2	6.0 ± 0.2	409.3 ± 32.4	5	203.3 ± 15.6	83.8 ± 22.1
0448-51900-0084	5004.9 ± 0.6	3.9 ± 0.5	239.1 ± 47.1	5009.9 ± 0.1	1.9 ± 0.1	164.6 ± 30.4	5	-	-
0452-51911-0080	5006.1 ± 0.1	2.6 ± 0.1	776.8 ± 19.7	5011.8 ± 0.1	1.7 ± 0.1	390.0 ± 17.9	5	21.2 ± 20.4	319.3 ± 20.0
0524-52027-0165	5002.4 ± 1.2	4.3 ± 0.7	143.0 ± 36.4	5010.3 ± 0.6	3.3 ± 0.3	136.9 ± 35.8	3	-	-
0555-52266-0033	5004.4 ± 0.3	2.8 ± 0.2	227.4 ± 25.4	5010.2 ± 0.3	2.8 ± 0.2	210.8 ± 26.4	5	-	-
0609-52339-0435	4997.7 ± 0.7	5.8 ± 1.0	93.6 ± 18.8	5009.3 ± 0.2	2.8 ± 0.2	74.7 ± 9.7	5	387.7 ± 69.4	311.2 ± 40.5

Notes. Column 1: Plate, MJD, Fiberid of spectroscopic observation; Column 2: the central wavelength of blue-shifted component of [O III] in units of Å; Column 3: corresponding second moment of blue-shifted component of [O III] in units of Å; Column 4: corresponding flux of blue-shifted component of [O III] in units of 10^{-17} erg/s/cm²; Column 5: the central wavelength of red-shifted component of [O III] in units of Å; Column 6: corresponding second moment of red-shifted component of [O III] in units of Å; Column 7: corresponding flux of red-shifted component of [O III] in units of 10^{-17} erg/s/cm²; Column 8: the confidence level (σ) of F-test; Column 9 and Column 10: the velocity offset of blue-shifted component and red-shifted component of [O III] determined by shifted velocity from SSP method in units of km/s, respectively, and ‘-’ represents an object with no obvious absorption line.

Table 5. Features of double-peaked narrow H α emission lines

Plate-Mjd-Fiberid (1)	λ_b (2)	σ_b (3)	F_b (4)	λ_r (5)	σ_r (6)	F_r (7)
0907-52373-0295	6559.33 ± 0.79	5.27 ± 0.96	136.39 ± 35.45	6568.32 ± 0.31	2.37 ± 0.35	60.61 ± 15.78
1048-52736-0416	6561.37 ± 0.26	2.57 ± 0.18	277.44 ± 25.33	6567.45 ± 0.26	2.34 ± 0.18	231.5 ± 25.08
1679-53149-0532	6560.57 ± 0.44	3.88 ± 0.28	422.8 ± 42.6	6568.22 ± 0.36	2.94 ± 0.25	264.44 ± 44.67
2022-53827-0553	6561.93 ± 0.5	2.98 ± 0.44	97.4 ± 13.99	6568.42 ± 0.3	1.94 ± 0.24	71.24 ± 12.52
2365-53739-0359	6561.19 ± 0.24	1.85 ± 0.17	144.58 ± 18.89	6566.42 ± 0.26	2.25 ± 0.2	195.86 ± 20.08
2791-54556-0005	6560.62 ± 0.44	3.5 ± 0.45	122.18 ± 15.51	6567.76 ± 0.34	1.75 ± 0.33	45.76 ± 11.71
3830-55574-0154	6564.2 ± 0.47	7.2 ± 0.31	596.14 ± 31.58	6572.06 ± 0.25	2.45 ± 0.4	63.97 ± 20.11
7723-58430-0620-	6563.42 ± 0.34	5.97 ± 0.23	616.97 ± 29.47	6571.56 ± 0.16	2.56 ± 0.23	131.63 ± 24.96
7875-56980-0296	6561.96 ± 0.13	1.87 ± 0.15	35.65 ± 3.05	6569.17 ± 0.14	1.87 ± 0.17	33.24 ± 3.66

Notes. Column 1: Plate, MJD, Fiberid of spectroscopic observation; Column 2: the central wavelength of blue-shifted component of narrow H α in units of Å; Column 3: corresponding second moment of blue-shifted component of narrow H α in units of Å; Column 4: corresponding flux of blue-shifted component of narrow H α in units of 10^{-17} erg/s/cm²; Column 5: the central wavelength of red-shifted component of narrow H α in units of Å; Column 6: corresponding second moment of red-shifted component of narrow H α in units of Å; Column 7: corresponding flux of red-shifted component of narrow H α in units of 10^{-17} erg/s/cm².

and the projected distance between two cores is about 4.7''. The galaxies are clearly undergoing interaction, while the scope of fiber position is not large enough to encompass the NLRs of both galaxies, after considering the 3'' in diameter of SDSS fibers.

SDSS J085457.23+544820.5 (Plate-Mjd-Fiberid: 0448-51900-0084) and SDSS J161950.67+500535.3 (Plate-Mjd-Fiberid: 2884-54526-0145) do not appear two cores, but large tidal tails in the southwest in the image.

SDSS J172120.48+263658.4 (Plate-Mjd-Fiberid: 0979-52427-0072) exhibits three cores in the image and the primary galaxy shows a large tidal tail. The NLR of the companion galaxy in the west of the primary galaxy should be out of the scope of fiber position (the projected distance between the two cores about 6.6''), while the NLR of the companion galaxy in the north of the primary galaxy may be covered by the scope of fiber position (the projected distance between the two cores about 3.0'').

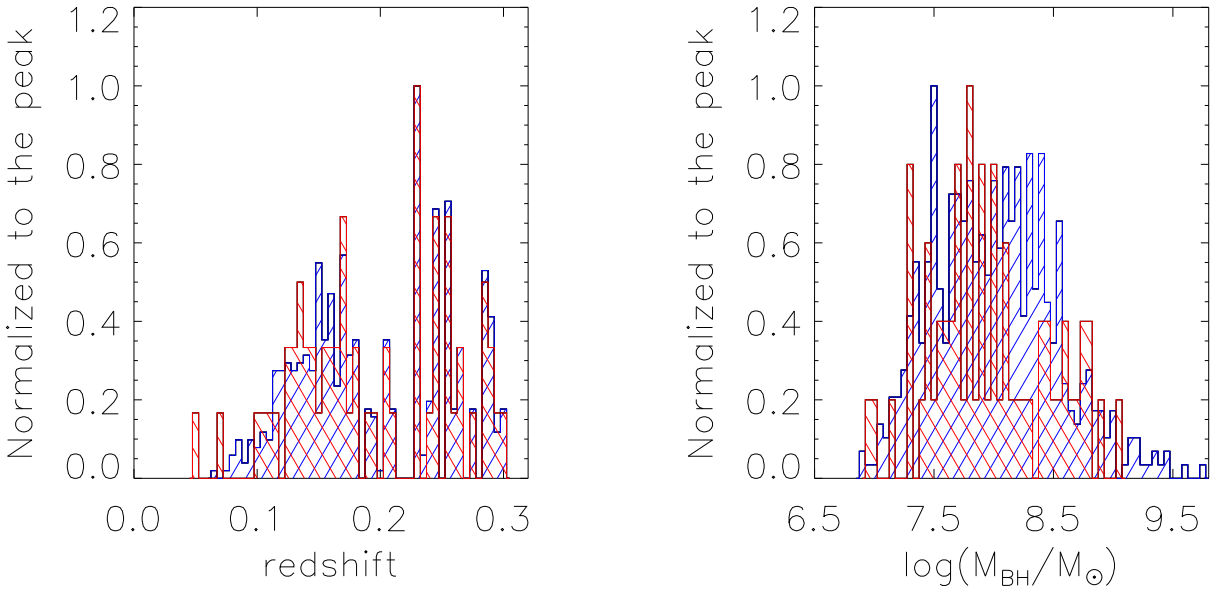


Figure 7. Distributions of redshift (left panel), black hole masses M_{BH} (right panel) for the 558 typical type 1 AGNs from Shen et al. (2011b) (histogram filled with blue line) and the 62 type 1 AGNs with double-peaked [O III] in our sample (histogram filled with red line).

SDSS J115638.15+150500.9 (Plate-Mjd-Fiberid: 1762-53415-0628) exhibits two cores with projected distance about 2.3'' in the image. The companion galaxy in the southeast is close to the primary galaxy, and its NLR may be encompassed by the scope of fiber position.

SDSS J141041.50+223337.0 (Plate-Mjd-Fiberid: 2785-54537-0499) shows two cores with projected distance about 4.0'' in the image, but the scope of fiber position is not large enough to encompass the NLR of the companion galaxy.

SDSS J222518.67+210203.6 (Plate-Mjd-Fiberid: 7582-56960-0660) shows a long and narrow companion galaxy in the southeast of the primary galaxy, and the projected distance between two cores is about 4.8''.

3.4. Properties of [O III]

The top-left panel of Figure 9 shows the distribution of the line width ratios of blue-shifted components to red-shifted components of [O III] with the mean value about 1.47 ± 0.27 . The top-middle panel of Figure 9 shows the distribution of the line flux ratios of blue-shifted components to red-shifted components of [O III] with the mean value about 1.63 ± 0.47 .

The top-right panel of Figure 9 shows the relationship between the redshifts and the peak separations of our double-peaked AGNs, and the Spearman Rank correlation coefficient is 0.36 with null-hypothesis probability of 0.44%. Objects at greater distance generally exhibit higher luminosities, and more luminous sources tend to have broader [O III] lines (Salviander et al. 2007). Consequently, larger peak separations are required to resolve double-peaked profiles. There-

fore, it is reasonable to expect an increase in observed peak separation with redshift. Our sample aligns with this trend, showing that at higher redshift, the typical peak separation tends to increase.

According to Kepler's law and the Magorrian relation (Magorrian et al. 1998; Marconi & Hunt 2003), the velocity offsets of [O III] blue-shifted/red-shifted components (V_b/V_r) have a negative dependence on their relative fluxes (F_b/F_r) for a dual AGN system, and it has been confirmed in Wang et al. (2009) through a study of type 2 AGNs with double-peaked [O III]. In the dual AGN scenario, the brighter shifted component, which is assuming typically from the more massive black hole, tends to be closer to the rotating center and has the lower orbital velocity. Since there are 26 type 1 AGNs with double-peaked [O III] in our sample showing no host galaxy contributions, it is hard to calibrate the precise redshift and then calculate the velocity offset of each component with respect to the absorption lines. The remaining 36 type 1 AGNs in our sample is considered to test the relationship between V_b/V_r and F_b/F_r . Here, the $V_b = |(\lambda_b - 5008.24) \times 3 \times 10^5 / 5008.24 + V_s|$ and $V_r = |(\lambda_r - 5008.24) \times 3 \times 10^5 / 5008.24 + V_s|$ are measured, where V_s is the shifted velocity determined by SSP method, and λ_b (λ_r) is the central wavelength of blue-shifted (red-shifted) component of [O III]. The relationship between V_b/V_r and F_b/F_r is shown in the bottom-left panel of Figure 9, and the Spearman Rank correlation coefficient is -0.34 with null-hypothesis probability of 4.23% after accepting the redshift

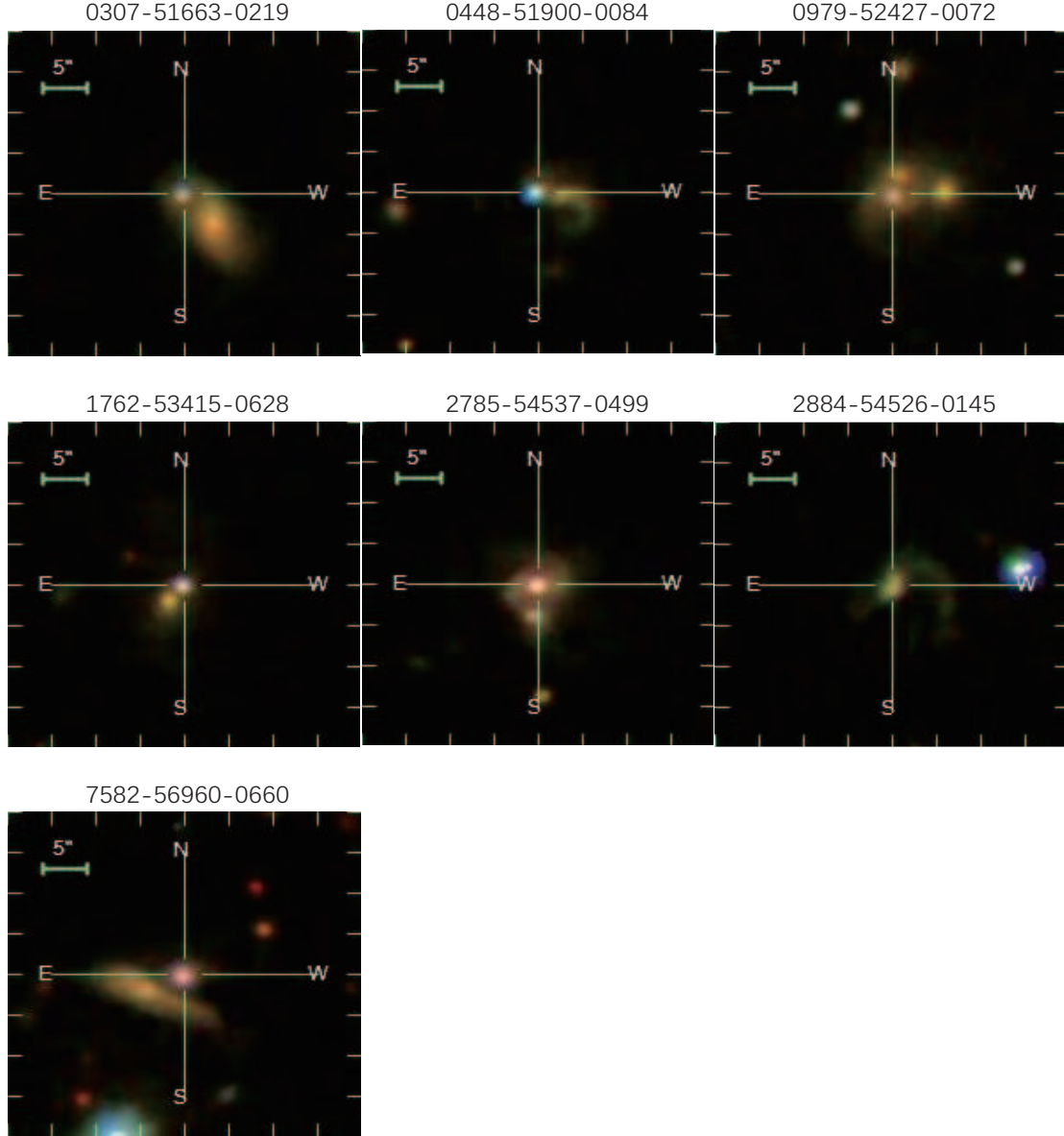


Figure 8. Photometric image properties of the seven type 1 AGNs with double-peaked [O III].

calibrated by the shifted velocity from the SSP method is accurate.

The bottom-middle panel of Figure 9 shows the relationship between the velocity offsets and line widths of blue-shifted components of double-peaked [O III] in our sample, and the Spearman Rank correlation coefficient is -0.03 with null-hypothesis probability of 86.93%. The bottom-right panel of Figure 9 shows the relationship between the velocity offsets and line widths of red-shifted components, and the Spearman Rank correlation coefficient is -0.08 with null-hypothesis probability of 64.73%. The velocity offset is almost independent of line width, which will provide clues on discussions on AGN outflow model to explain the double-peaked profiles.

4. DISCUSSION

In this section, the basic properties of double-peaked [O III] in the previous sections are synthesized to analyze the probable physical scenarios that produce double-peaked [O III], such as superposition, AGN outflows, dual AGN and rotating disk.

4.1. Superposition

In this scenario, along the same line-of-sight, the blue-shifted emission lines originate in the foreground QSO, while the red-shifted emission lines are associated with another background object (Decarli et al. 2014). However, it is hard for two systems with small separation in spatial and velocity to be unrelated. Komossa et al. (2008) thought the possi-

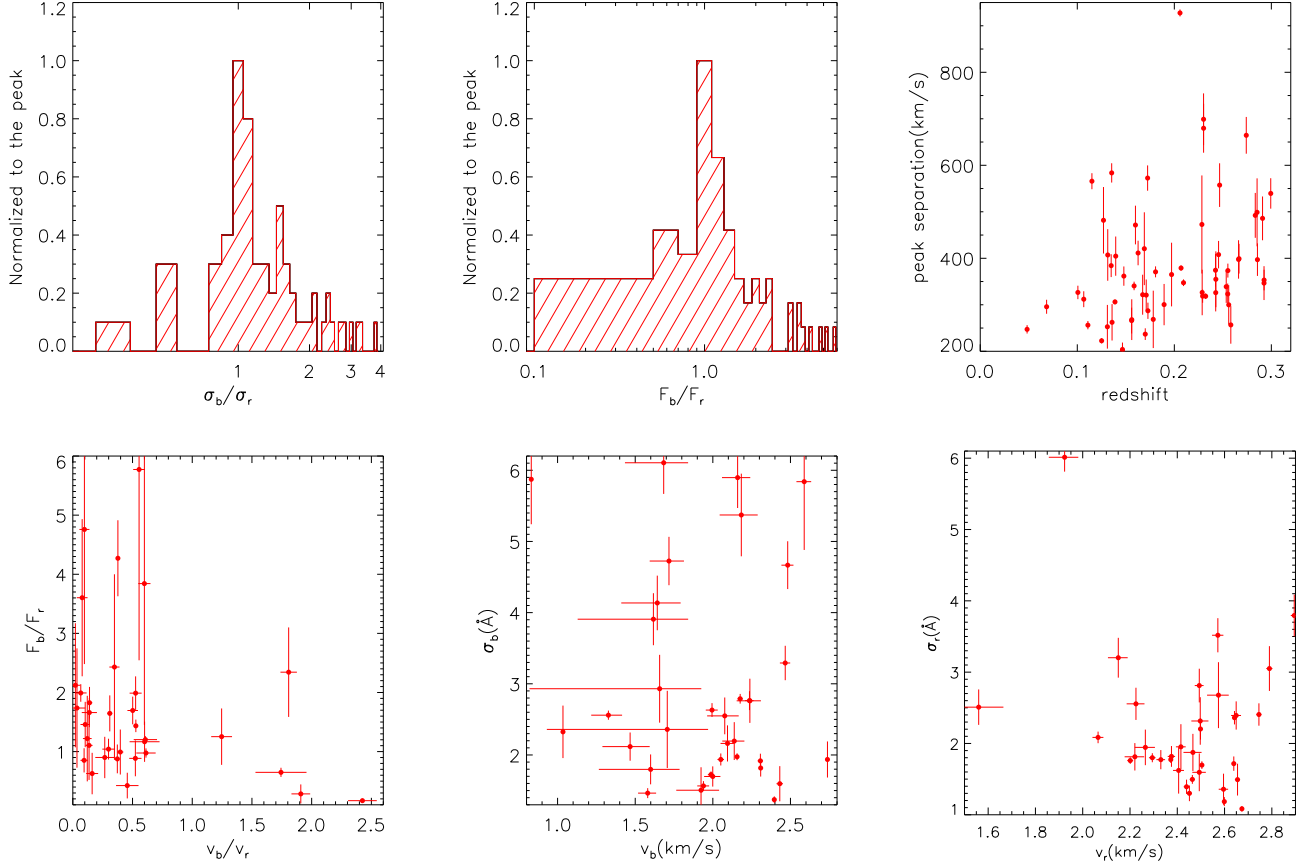


Figure 9. Top-left panel: the distribution of line width of the blue-shifted/red-shifted [O III] components (σ_b/σ_r); Top-middle panel: the distribution of line flux ratio (F_b/F_r); Top-right panel: the relationship between peak separations and redshifts; Bottom-left panel: the relationship between V_b/V_r and F_b/F_r ; Bottom-middle panel: the relationship between V_b and σ_b ; Bottom-right panel: the relationship between V_r and σ_r .

bility of a chance superposition is considerably improbable. Shields et al. (2009) estimated that the probability of superposition within 1 arcsec (observed in the same SDSS fiber) of two systems with velocity offset less than 2650 km/s is about 10^{-8} for a given QSO. In order to increase the almost negligible probability of superposition, the QSO is assumed to superimposed within rich galaxy clusters (Heckman et al. 2009; Shields et al. 2009). Based on this assumption, Shields et al. (2009) proposed that the probability of a chance superposition within 1 arcsec (observed in the same SDSS fiber) is $10^{-4.3}$, and then this prediction is confirmed by Dotti et al. (2010).

Considering the 11557 AGNs in our parent sample, it is hard to find even one object with a chance superposition due to the low probability. But it is hard to totally rule out the superposition scenario, in the near future, detecting SDSS spectrum with potential two sets of absorption line systems should be an interesting objective to support probable superposition.

4.2. AGN outflows

AGN outflows (Duric & Seaquist 1988; Whittle & Wilson 2004; Yao et al. 2021) are able to produce double-peaked profiles. Powerful AGNs are accepted to be capable of driving large-scale outflows. NGC 1068 (Seyfert 2) (Axon et al. 1998; May & Steiner 2017) is a prototypical case which has double-peaked emission lines caused by outflows. In the scenario of bi-conical outflows, the blue-shifted and red-shifted components of double-peaked [O III] profiles are determined by the projection of outflows moving toward and away from the observer. As shown in Table 1 and Table 6 in Appendix B, there are 11 radio loud AGNs in our sample based on the calculated R , and the fraction of the type 1 AGNs with radio fluxes in our final sample is two times larger than the parent sample.

If generally accepted that peak separation in NLR is produced by outflows, the NLR around the AGNs should be stratified. If the double-peaked profiles of narrow emission lines originate from distinct regions, it would naturally result in variations in peak separations and line widths. In another words, in the radially decelerating outflow of NLR,

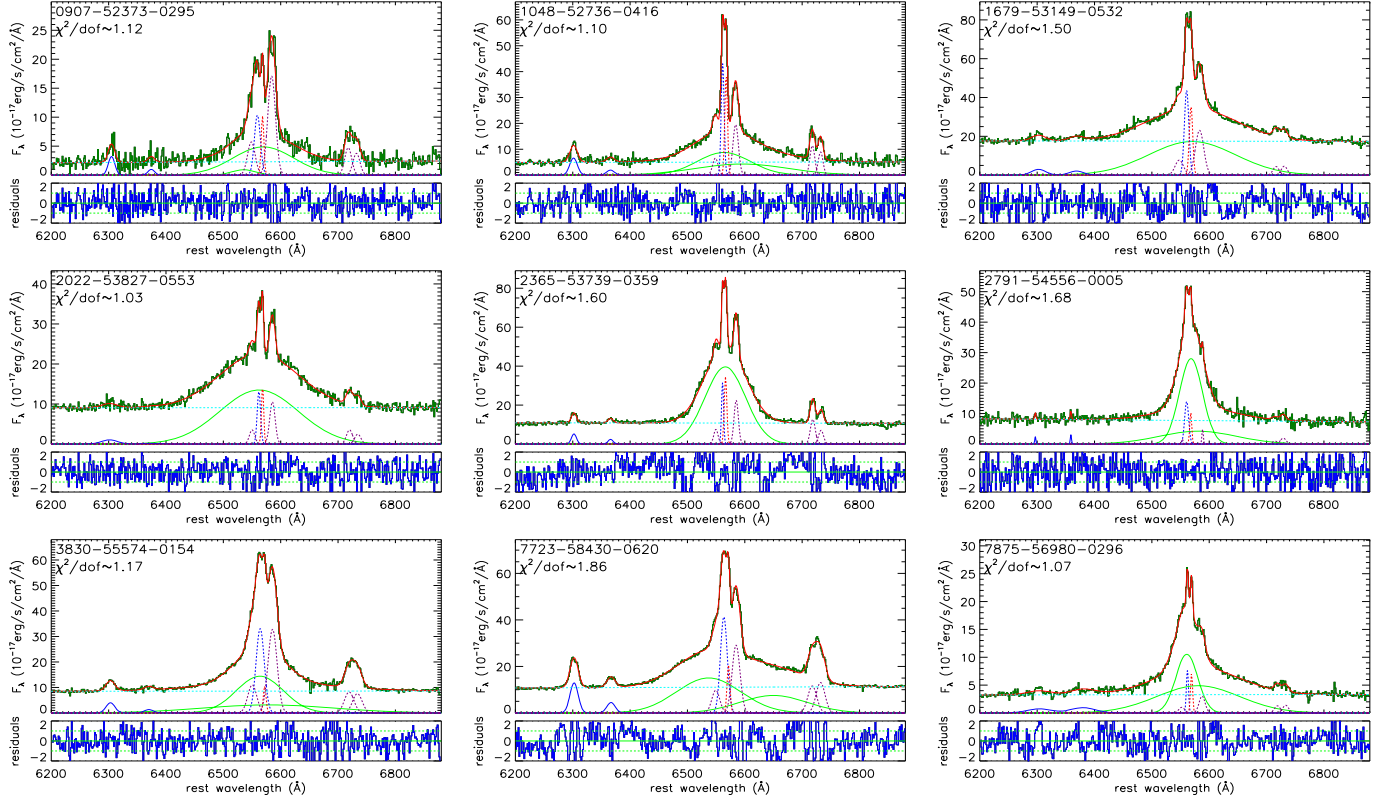


Figure 10. The best fitting results of the emission lines around double-peaked narrow H α emission lines. In the top of each panel, the solid dark green line shows the line spectrum after subtracting starlight (if present) determined from host galaxy with Plate-Mjd-Fiberid shown in the top-left of corner, the solid red line represents the best fitting results with χ^2/dof shown in the top-left of corner, the dashed cyan line represents continuum emission, the dashed purple lines represent [N II] and [S II] doublets, the solid green lines represent broad H α emission line, and the dashed blue line and red line represent the blue-shifted and red-shifted components of narrow H α , respectively. In the bottom of each panel, the solid blue line represents the residuals calculated by the line spectrum minus the best fitting results and then divided by uncertainties of SDSS spectrum. The horizontal solid and dashed green lines show residuals=0, ± 1 , respectively.

the emission lines produced closer to the AGNs would exhibit higher velocity offsets, and more broadened line widths, which is dominated by the bulge gravitational potential (Barrows et al. 2013). The correlation between peak separation and line width can be found in Komossa et al. (2008); Liu et al. (2010a). By contrast, there is a very weak correlation between line widths and velocity offsets in both blue-shifted and red-shifted components of [O III], as shown in Figure 9. So the physical explanations for the velocity offsets in our sample are likely different from the samples in Komossa et al. (2008); Liu et al. (2010a).

When the outflow axis is oriented at an intermediate angle between edge-on and face-on, the red-shifted component is expected to be more attenuated than the blue-shifted component. The portions of the NLR with the highest line-of-sight velocity components are likely to be the most heavily obscured, while those with the smallest line-of-sight velocity components experience relatively less obscuration, unless there is asymmetrical obscuration.

According to the top-middle panel of Figure 9, it appears that the mean value of line flux of the blue-shifted compo-

nents is generally larger than that of the red-shifted components, consistent with the notion above. However, the V_b and V_r should be similar in the symmetrical outflows, which is inconsistent with the negative correlation between V_b/V_r and F_b/F_r .

4.3. Dual AGN

It is possible that AGNs may host two black holes following a galaxy merger, through tidal interactions, and galaxy merger is effective at enhancing nuclei activity by funneling dust and gas toward potential of each black hole (Comerford et al. 2009b; Barrows et al. 2012). In this scenario, each nucleus may possess its own NLR and the double peak may be from two distinct NLRs, which will move with its own active black hole. Therefore, it will be expected that there are two sets of narrow emission lines from two distinct NLRs and each set of narrow emission lines has similar redshift. So we recheck the narrow H α emission line in our sample and find nine objects exhibiting obvious double peak. The spectra of the nine objects around H α emission line are refit and the fitting parameters are done similar as before, excepting two Gaussian

functions applied to describe narrow H α emission lines. The fitting results are shown in Figure 10 and the corresponding model parameters of the emission lines are listed in Table 5, and all the nine objects show similar velocity offsets in blue-shifted (red-shifted) components of narrow H α and [O III] narrow emission lines. Here, the object with offset between [O III] and narrow H α emission line in velocity space less than 100 km/s is considered as having similar velocity offset.

Meanwhile, if some narrow emission lines in one set are obscured and only the other set of narrow emission lines can be fully observed, the single-peaked narrow emission line should have same velocity offset with one of the double peak of [O III]. Therefore, we put single-peaked H α emission line and double-peaked [O III] in velocity space and found 31 objects exhibit coincident velocity offsets in H α and either of blue-shifted and red-shifted components of [O III] emission lines, and 22 objects show different velocity offsets between H α and both blue-shifted and red-shifted components of [O III]. Similarly, the object with offset between one set of [O III] and narrow H α emission line in velocity space less than 100 km/s is considered as having similar shift. Here, we show an example of the 53 objects with single-peaked narrow H α emission line in Figure 11, and the best fitting results to all the 53 targets are shown in Figure 15 in Appendix A.

Meanwhile, there are also two objects showing tidal tails, which might be caused by merger, four objects showing clear two cores and one object showing three cores in the images. However, For the objects (Plate-Mjd-Fiberid: 0307-51663-0219, 2785-54537-0499 and 7582-56960-0660), the two cores of the objects are so far that the scope of fiber position can hardly cover both NLRs of two cores. Even for the objects (Plate-Mjd-Fiberid: 0979-52427-0072 and 1762-53415-0628) with NLRs of two nearest cores covered in the scope of fiber position, the double-peaked [O III] also can be produced by other models related to a single AGN rather than a dual AGN, as discussed in [Zhang & Zheng \(2023\)](#); [Maschmann et al. \(2023\)](#).

Although most sources do not show two cores or merger in the images, they cannot be completely ruled out as dual AGNs. In our case, with a mean redshift of $z \sim 0.195$, the 1-arcsec limit for unresolved objects corresponds to approximately 3.3 kpc. This suggests that spatial resolution constraints may lead to some dual cores being optically unresolved in images.

Moreover, the profiles of broad H α emission lines in our sample might be determined by two broad line regions in dual AGNs. So the line widths and line fluxes of broad H α emission lines in dual AGNs tend to be broader and larger than those in normal type 1 AGNs, and then it is expected to see larger black hole masses of dual AGNs than normal AGNs. However, through Student's t-test statistical technique, we find no significant difference in black hole masses between type 1 AGNs with DPNELs in our sample and normal type 1

AGNs in [Shen et al. \(2011b\)](#), which is at odds with dual AGN systems.

4.4. Rotating disk

In purely geometrical terms, the model is consisted of a flat extended disk component plus a spherical core component ([Xu & Komossa 2009](#)). The blue-shifted and red-shifted narrow emission lines would arise in the classical NLR, which follows a strict disk geometry ([Greene & Ho 2005a](#)) and the extended emission lines, if exist, are produced in spherical very inner part of the NLR (or outer broad line region). The shape of the lines and relative positions of the peaks are dependent on the orientation of the disk plane and the disk outer radius ([Barrows et al. 2012](#)). Based on axisymmetric models of rotating disk, [Maschmann et al. \(2023\)](#) found that the double-peaked profiles primarily depend on the observation angle: as the inclination increases, the separation between the peaks becomes larger. As discussed in [Smith et al. \(2012\)](#), two peaks of the [O III] line with nearly equal intensities often represent rotating disks. In addition, the great similarity of the line flux ratio ($0.75 \leq F_b/F_r \leq 1.25$, as shown in [Smith et al. 2012](#)) in the blue-shifted and red-shifted narrow emission lines hints only a single ionizing continuum and similar physical condition (e.g., cloud densities, column densities and metal abundances) in the NLR.

However, the symmetric rotating disk model cannot account for the larger mean line flux of the blue-shifted components compared to the red-shifted components in our sample. This case, however, can be explained by a lopsided disk, as found in [García-Burillo et al. \(2003\)](#). Our findings do not rule out the possibility of an asymmetric disk configuration.

4.5. future applications

Although the cause of the double-peaked [O III] can be initially judged according to the current results, different models are not completely at odds with each other. Therefore, it is hard to give a unique explanation for double-peaked [O III] of each object. But at least the 22 objects in our sample with different velocity offsets between double-peaked [O III] and narrow H α emission lines could be excluded as dual AGN candidates. If possible, more observational information, such as high-resolution imaging and long-slit spectroscopy should be obtained to provide further information on the NLRs in order to determine the cause of the double-peaked [O III] properties in the future.

Future work will focus on investigating differences in long-term variability between the 62 type 1 AGNs with double-peaked [O III] in our sample and normal type 1 AGNs. These analyses aim to provide deeper insights into the physical mechanisms responsible for the observed double-peaked features and their connections to AGN variability and orientation effects.

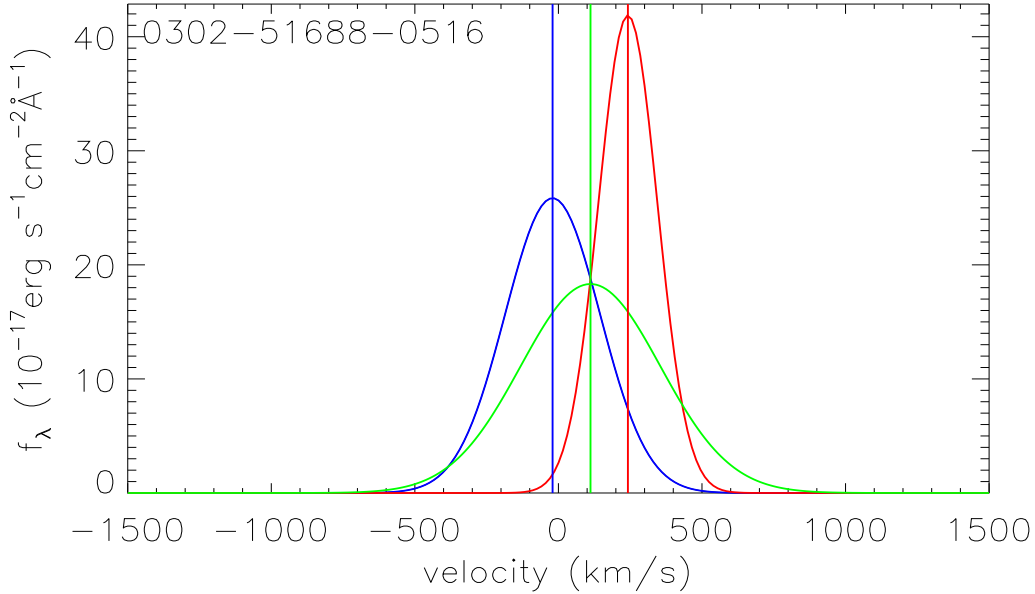


Figure 11. An example of the offsets of [O III] and narrow H α emission lines the object with single-peaked narrow H α emission lines in our sample in velocity space. The solid blue line represents the determined blue-shifted component of [O III], and the vertical blue line marks the position of the central wavelength of the blue-shifted component of [O III], the solid red line represents the determined red-shifted component of [O III], and the vertical red line marks the position of the central wavelength of the red-shifted component of [O III], the solid green line shows the determined narrow H α component, and the vertical green line marks the position of the central wavelength of the narrow H α .

The new sample presented in this work provides a significant update to the catalog of type 1 AGNs with double-peaked [O III], introducing 47 previously unreported objects. This expanded sample could serve as an important complement to studies of type 2 AGNs with double-peaked [O III] (selected using similar criteria), enabling a more comprehensive investigation of AGN activity.

Additionally, a separate sample of 25 type 1.9 AGNs (AGNs with broad H α but no broad H β emission line due to extinction) is excluded during the fifth step in Section 2. This sample holds potential for studying the effects of line-of-sight orientation on the observed double-peaked [O III] profiles.

5. SUMMARY AND CONCLUSIONS

We systematically select candidates of type 1 AGNs with double-peaked [O III] of spectra through strict criteria from 11557 QSOs at $z < 0.3$ in SDSS DR16. After visual check and Gaussian fitting of [O III], fitting of broad H α emission lines, F-test for [O III] emission lines and check of broad H β and [O III] emission lines, a sample of 62 type 1 AGNs with double-peaked [O III] is built. The main summary and conclusions are shown as follows.

- The fraction of type 1 AGNs with double-peaked [O III] in the final sample is about 0.5% of the parent QSO sample.

- Among the 62 type 1 AGNs, there are 26 objects without host galaxy contributions and 36 objects showing host galaxy contributions.
- The Fe II emission lines around [O III] emission lines may affect our sample selection, and the components of Fe II emission lines should be determined to avoid the influence on double-peaked [O III].
- The mean value of the black hole masses for the 62 type 1 AGNs is about $\log M_{\text{BH}}/M_\odot \sim 7.96 \pm 0.05$, and the result is statistically similar to normal type 1 AGNs, which is inconsistent with dual AGN model.
- There are 35% of type 1 AGNs with double-peaked [O III] in the FIRST footprint detected with radio fluxes, while only 16% of parent sample is detected with radio fluxes. In addition, 11 type 1 AGNs in our final sample are radio loud AGNs.
- There are seven AGNs exhibiting sign of merger with four objects showing two cores, one object showing three cores and two objects showing tidal tails in the images.
- The line widths and line fluxes of the blue-shifted components are larger than these of red-shifted components.

- There is a trend in our sample that the observed peak separations increase with redshifts, and the Spearman Rank correlation coefficient is 0.36.
- Considering the negligible probability of superposition model, it is hard to find the double-peaked [O III] in our sample produced by chance superposition.
- There is a very weak correlation between the line widths and velocity offsets in both blue-shifted and red-shifted components of [O III], which disfavors AGN outflow model.
- There is a negative relationship between V_b/V_r and F_b/F_r with the Spearman Rank correlation coefficient of -0.34, which is consistent with dual AGN model.
- Among the 62 type 1 AGNs with double-peaked [O III], there are nine type 1 AGNs with double-peaked profiles in both [O III] and H α emission lines, and all of the nine AGNs show similar velocity offsets between blue-shifted (red-shifted) components of [O III] and H α emission lines. In addition, in the remaining 53 type 1 AGNs with single-peaked narrow H α emission lines, 31 AGNs exhibit coincident velocity offsets in narrow H α and one shifted component of [O III], and 22 AGNs

show different velocity offsets between H α and double-peaked [O III], which can be excluded as dual AGN candidates.

- The similar line flux ratio in the blue-shifted and red-shifted components of [O III] may hints only a single ionizing continuum (symmetric rotating disk model), and the larger mean value of line flux of the blue-shifted component than that of red-shifted component in our sample would be possible in the asymmetric case.

The current findings do not strongly favor any single explanation, and additional observational data would be beneficial to better understand the details of NLRs. This work offers a significant update to the sample of type 1 AGNs with double-peaked [O III], introducing 47 newly identified type 1 AGNs.

ACKNOWLEDGMENTS

This work is supported by the National Natural Science Foundation of China (Nos. 12173020, 12373014, 12273013). This manuscript has made use of the data from the Sloan Digital Sky Survey (SDSS). The SDSS DR16 web site is (<http://skyserver.sdss.org/dr16/en/home.aspx>). The MPFIT website is (<http://cow.physics.wisc.edu/~craigm/idl/idl.html>). The FIRST website is (<http://sundog.stsci.edu/index.html>).

APPENDIX

A. SPECTRA OF THE 62 TYPE 1 AGNS

The SDSS spectra of the 62 type 1 AGNs in our final sample are shown in Figure 12, and the best fitting results of the emission lines around H α and [O III] are shown in Figure 13 and 14, respectively. The offsets of [O III] and narrow H α emission lines in velocity space are shown in Figure 15.

REFERENCES

- Arzoumanian, Z., Baker, P. T., Blumer, H., et al., 2020, ApJ, 905, 34
 Ahumada, R., Allende Prieto, C., Almeida, A., et al., 2020, ApJS, 249, 3
 An, T.; Paragi, Z.; Frey, S., et al, 2013, MNRAS, 433, 1161
 Ananna, T. T., Weigel, A. K., Trakhtenbrot, B., et al., 2022, ApJS, 261, 9
 Axon, D. J.; Marconi, A.; Capetti, A., et al, 1998, ApJ, 496, 75
 Barrows, R.S.; Stern, D.; Madsen, K., et al, 2012, ApJ, 744, 7
 Barrows, R. S., Sandberg Lacy, C. H., Kennefick, J., et al, 2013, ApJ, 769, 95
 Barrows, R. S., Comerford, J. M., Greene, J. E., et al., 2016, ApJ, 829, 37
 Becker, R. H.; White, R. L.; Helfand, D. J., 1995, ApJ, 450, 559
 Bentz, M. C. et al., 2013, ApJ, 767, 149
 Bhattacharya, A.; Nehal, C. P.; Das, M., et al., 2023, MNRAS, 524, 4482
 Bruzual, A. G.; Charlot, S., 1993, ApJ, 405, 538
 Bruzual, G.; Charlot, S., 2003, MNRAS, 344, 1000
 Cappellari, M., 2017, MNRAS, 466, 798
 Chilingarian, I. V., Zolotukhin, I. Y., Katkov, I. Y., et al., 2017, ApJS, 228, 14
 Cid Fernandes, R.; Mateus, A.; Sodré, L., et al., 2005, MNRAS, 358, 363
 Comerford, J. M.; Griffith, R. L.; Gerke, B. F., et al., 2009a, ApJ, 702, 82
 Comerford, J.M.; Gerke, B.F.; Newman, J.A., et al, 2009b, ApJ, 698, 956
 Comerford, J. M., Pooley, D., Gerke, B. F., et al., 2011, ApJ, 737, 19

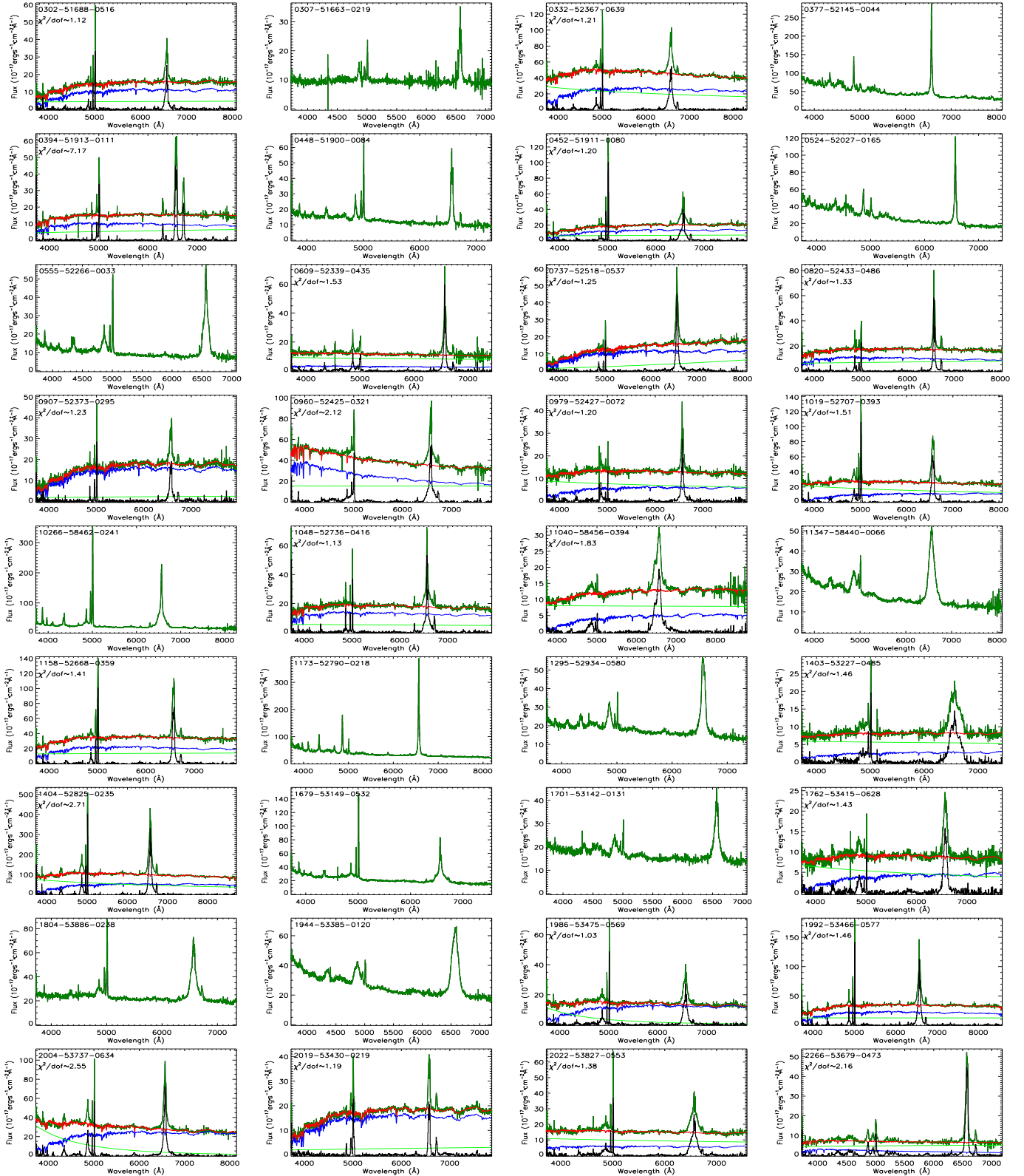


Figure 12. The SDSS spectra of the 62 type 1 AGNs in the final sample. In each panel, the solid dark green line represents the spectrum with Plate-Mjd-Fiberid shown in the top-left of corner, the solid red line shows the best fitting results with χ^2/dof (if present) shown in the top-left of corner, the solid blue line shows starlight (if present), the solid green line represents the AGN continuum emission, and the solid black line represents the line spectrum calculated by the SDSS spectrum minus the best fitting results (if present).

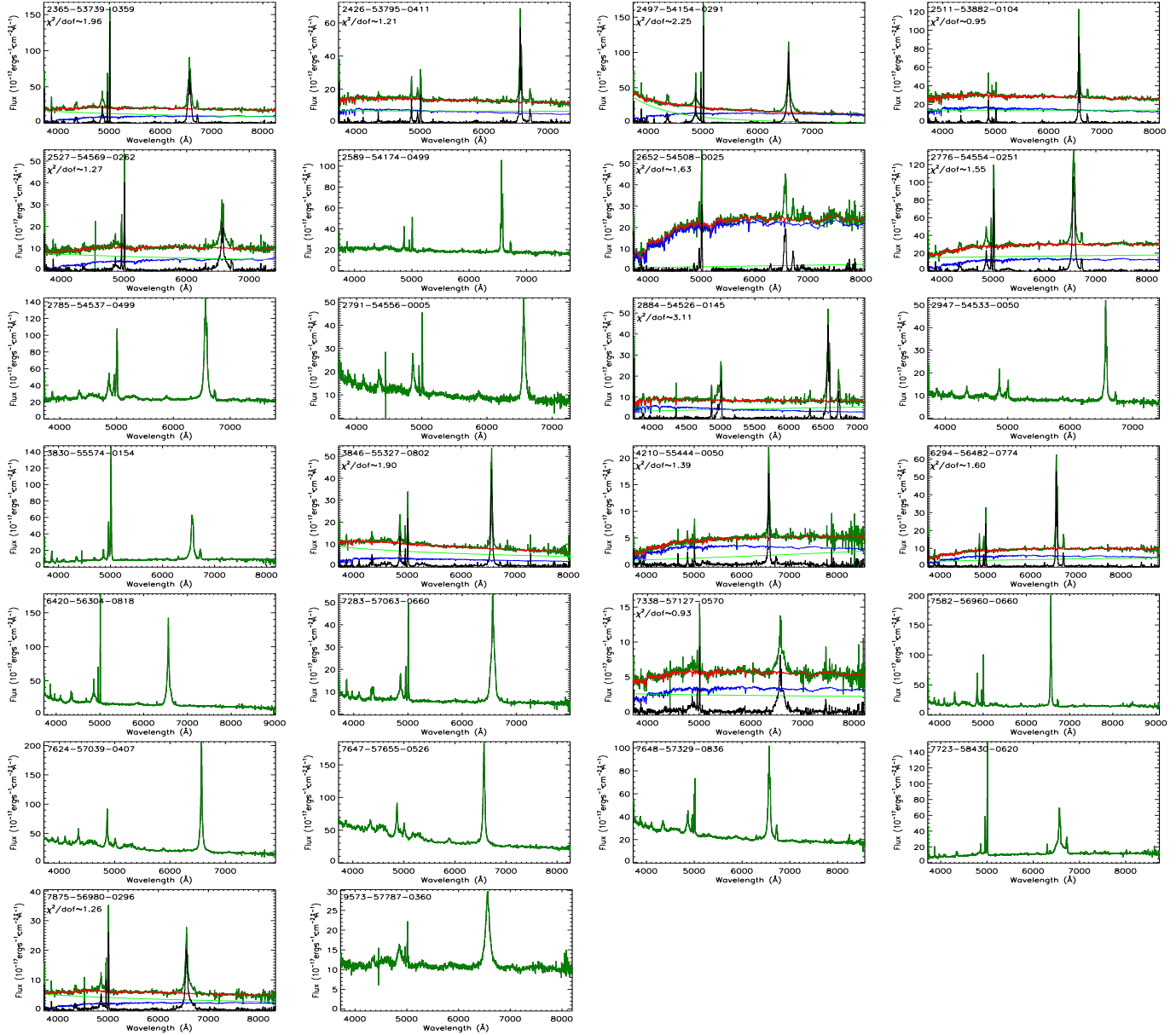


Figure 12. – to be continued

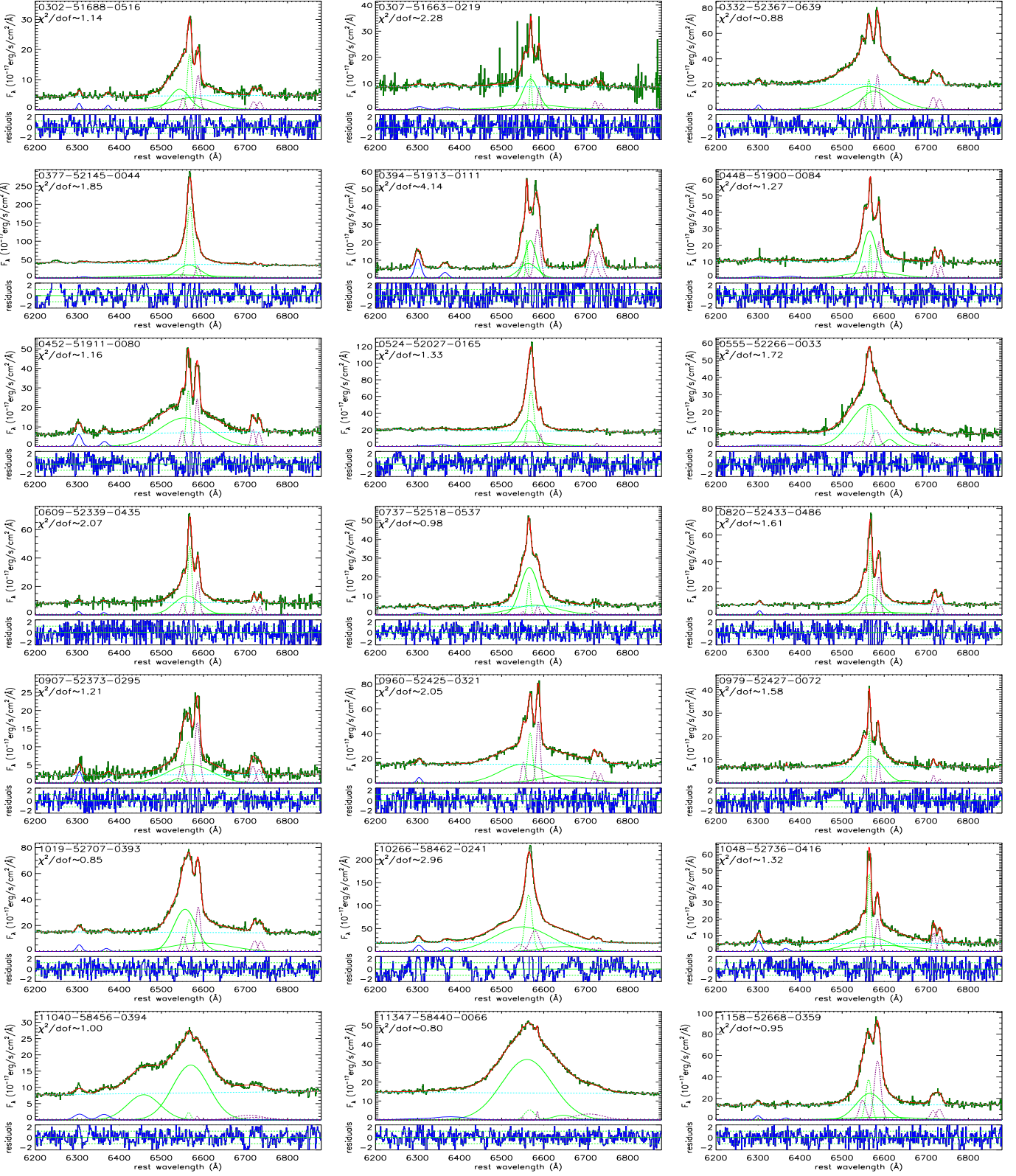


Figure 13. The best fitting results of the emission lines around H α . In the top of each panel, the solid dark green line shows the line spectrum after subtracting starlight (if present) from host galaxy with Plate-Mjd-Fiberid shown in the top-left of corner, the solid red line represents the best fitting results with χ^2/dof shown in the top-left of corner, the dashed cyan line represents continuum emission, the solid green lines represent the determined components of broad H α emission line, the dashed green line represents narrow H α emission line, the solid blue lines represent [O I] emission lines (if present), and the dashed purple lines represent [N II] and [S II] doublets. In the bottom of each panel, the solid blue line represents the residuals calculated by the line spectrum minus the best fitting results and then divided by uncertainties of SDSS spectrum, the horizontal solid and dashed green lines show residuals=0, ± 1 , respectively.

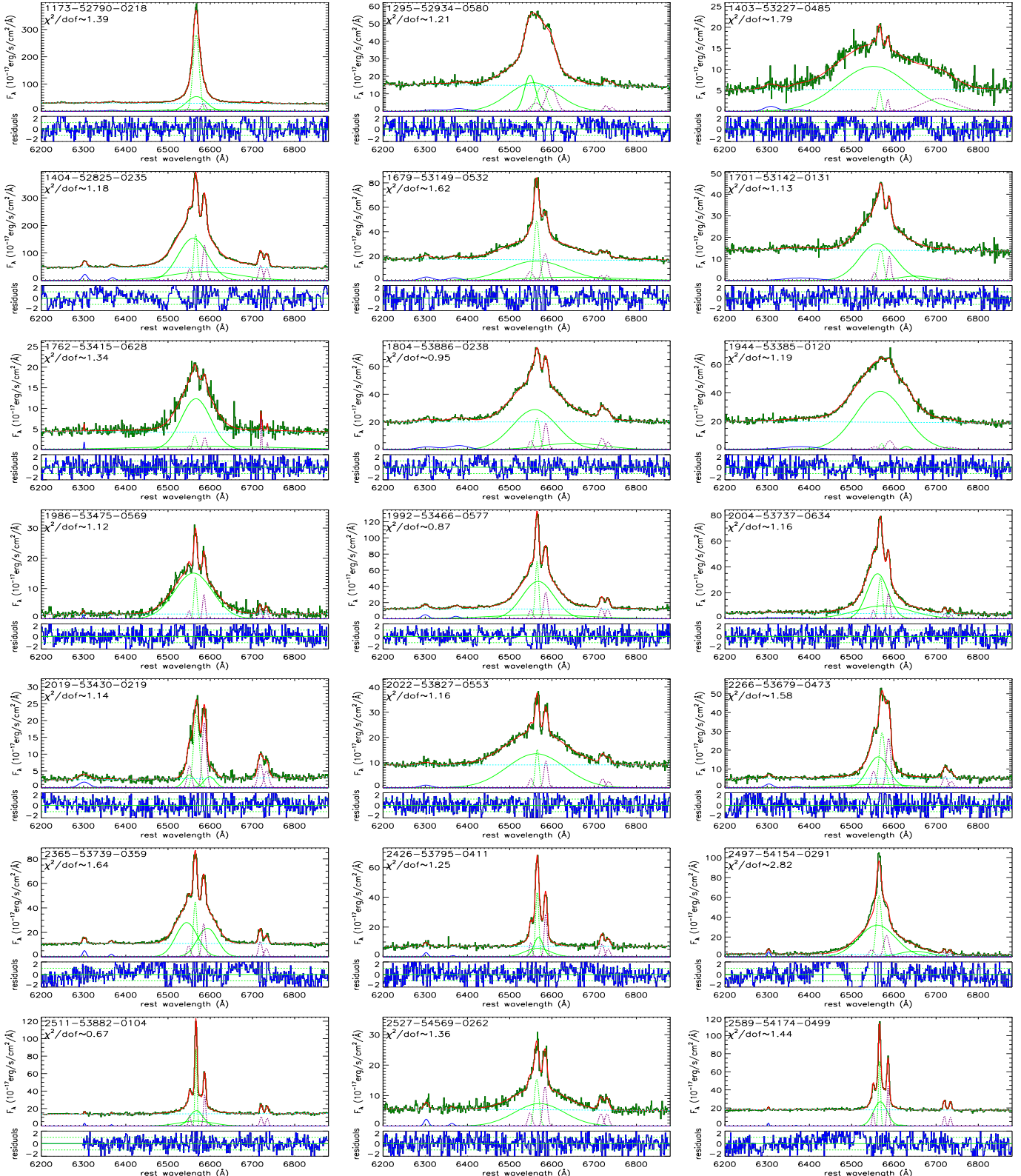


Figure 13. – to be continued

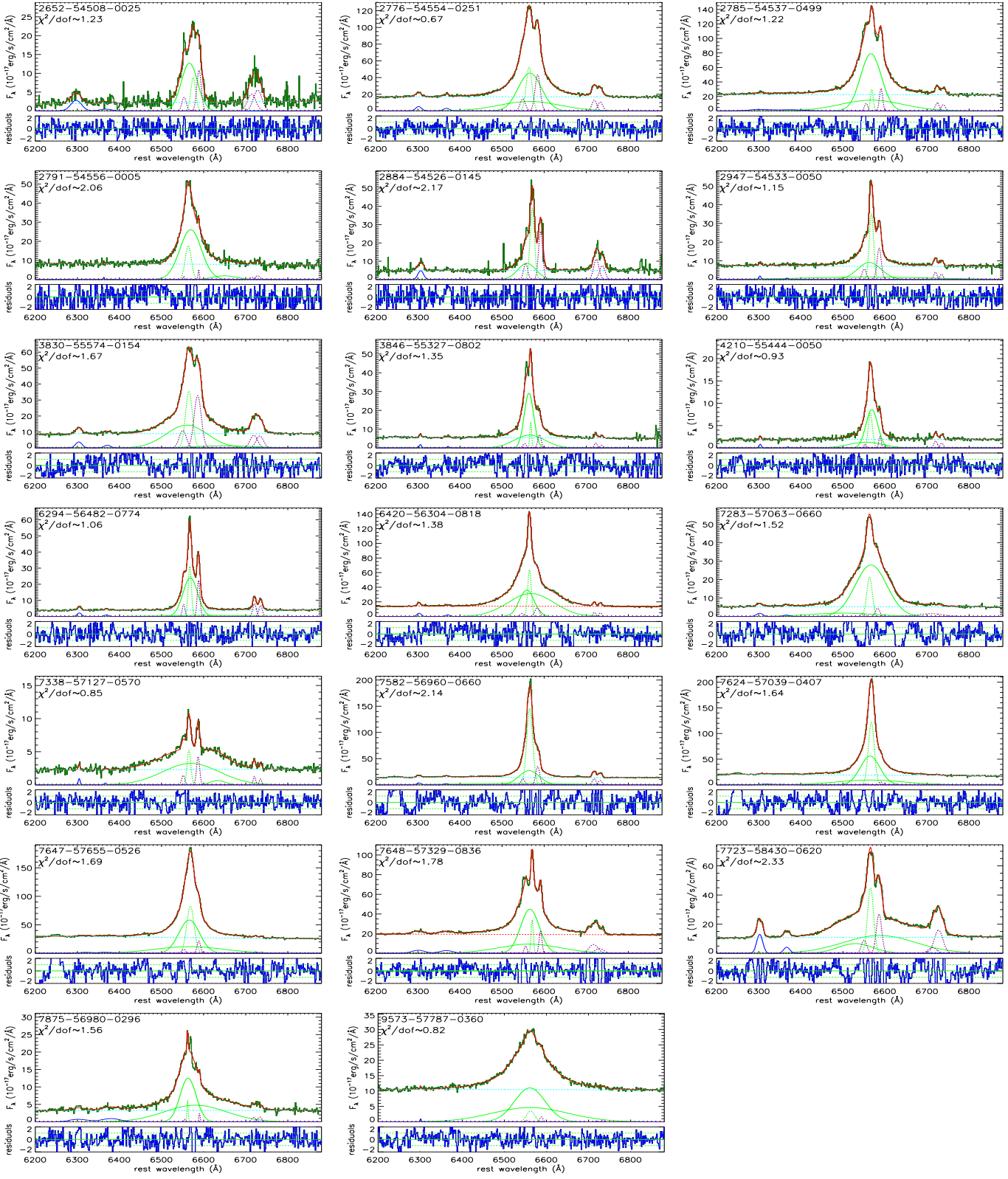


Figure 13. – to be continued

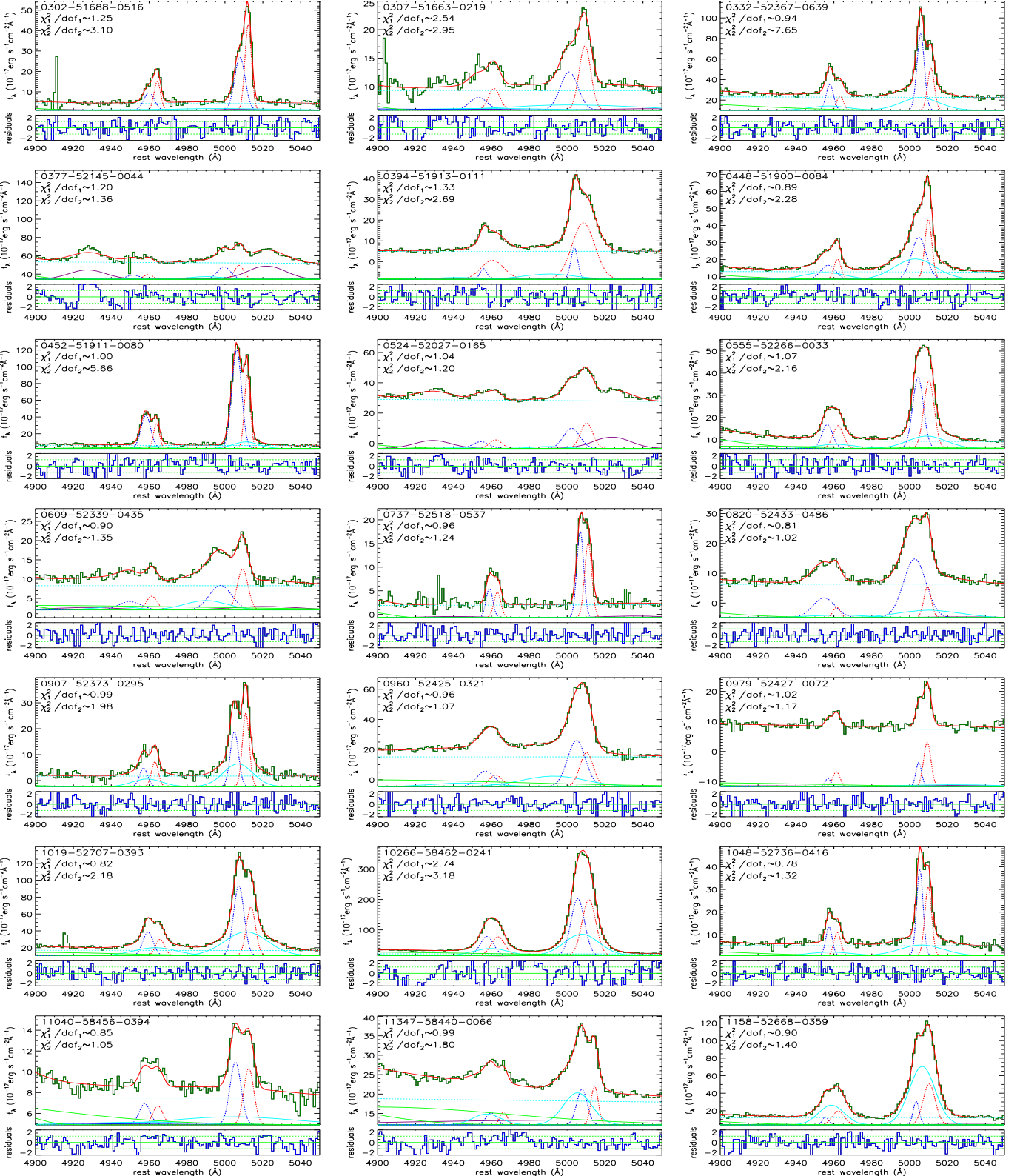


Figure 14. The best fitting results of the emission lines around [O III]. In the top of each panel, the solid dark green line shows the line spectrum after subtracting starlight (if present) determined from host galaxy with Plate-Mjd-Fiberid shown in the top-left of corner, the solid red line represents the best fitting results with two narrow Gaussian functions describing each core component of [O III] doublet, and the corresponding χ^2_1/dof_1 is shown in the top-left of corner, the χ^2_2/dof_2 determined by one narrow Gaussian function for each core component of [O III] doublet is shown in the top-left of corner, the dashed cyan line represents continuum emission, the solid purple lines represent Fe II emission lines, the solid green lines represent broad H β emission line, the solid cyan lines represent extended component of [O III], and the dashed blue and red lines represent the blue-shifted and the red-shifted components of [O III], respectively. In the bottom of each panel, the solid blue line represents the residuals calculated by the line spectrum minus the best fitting results and then divided by the uncertainties of the SDSS spectrum, the horizontal solid and dashed green lines show residuals=0,±1, respectively.

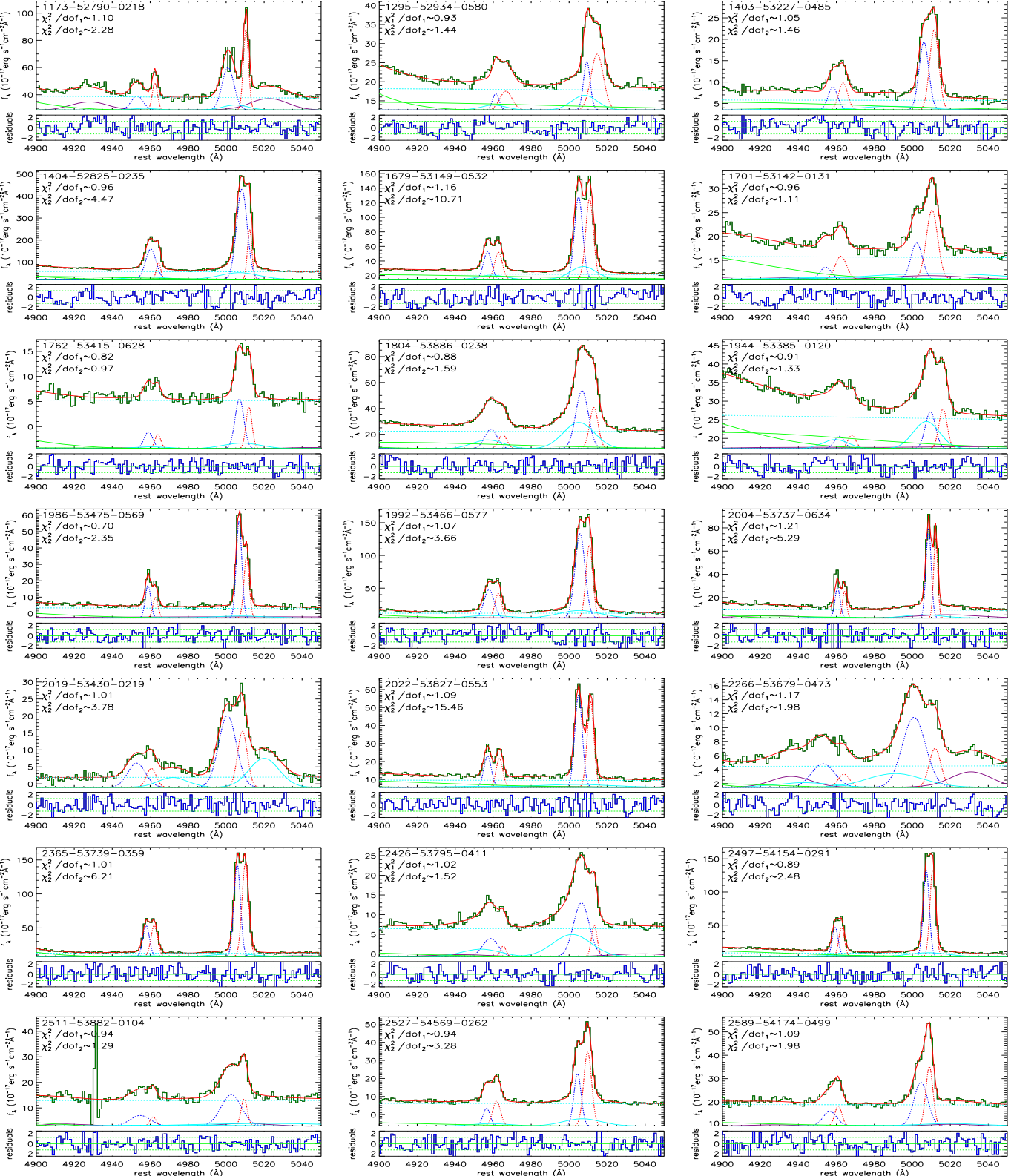


Figure 14. – to be continued

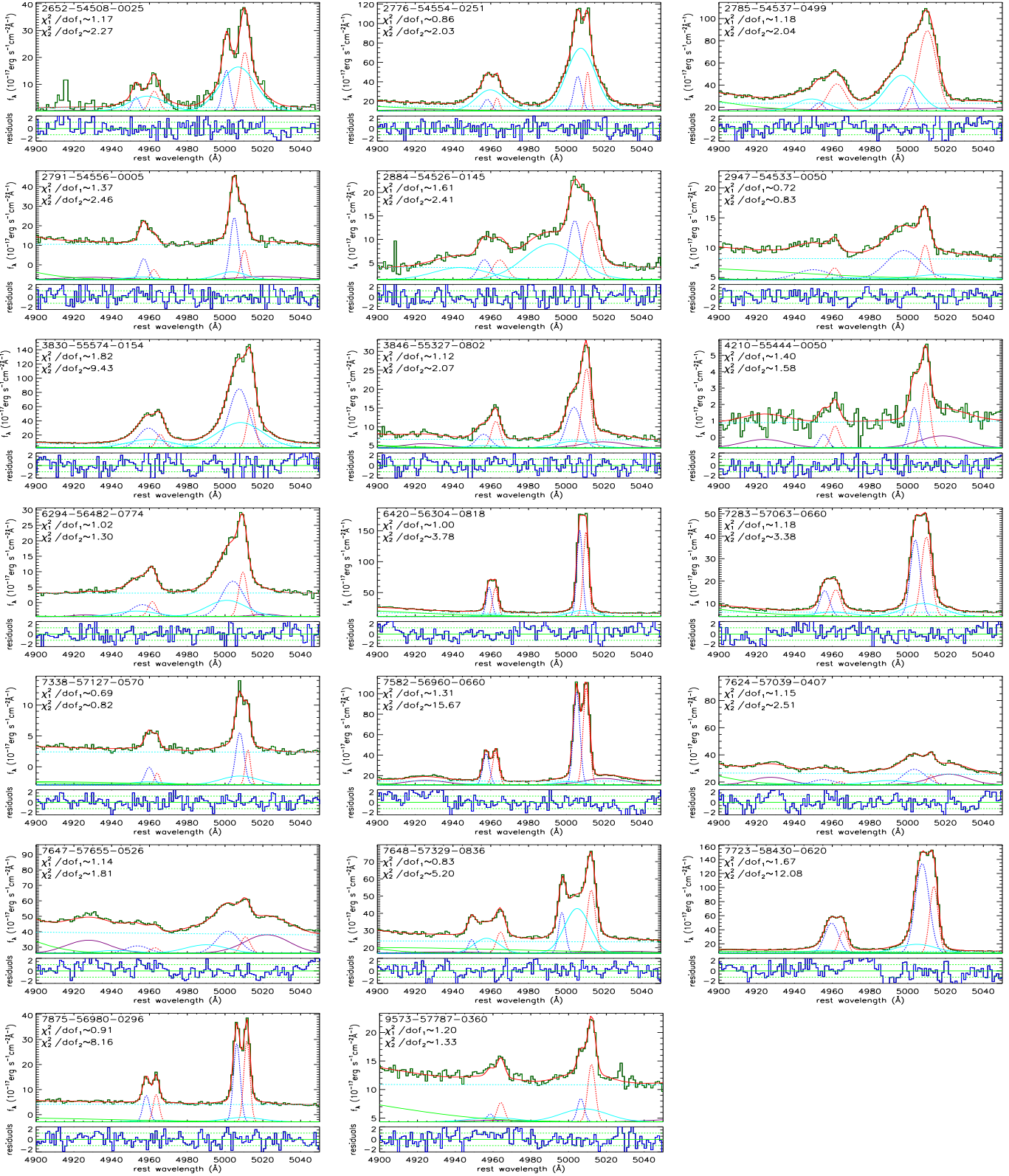


Figure 14. – to be continued

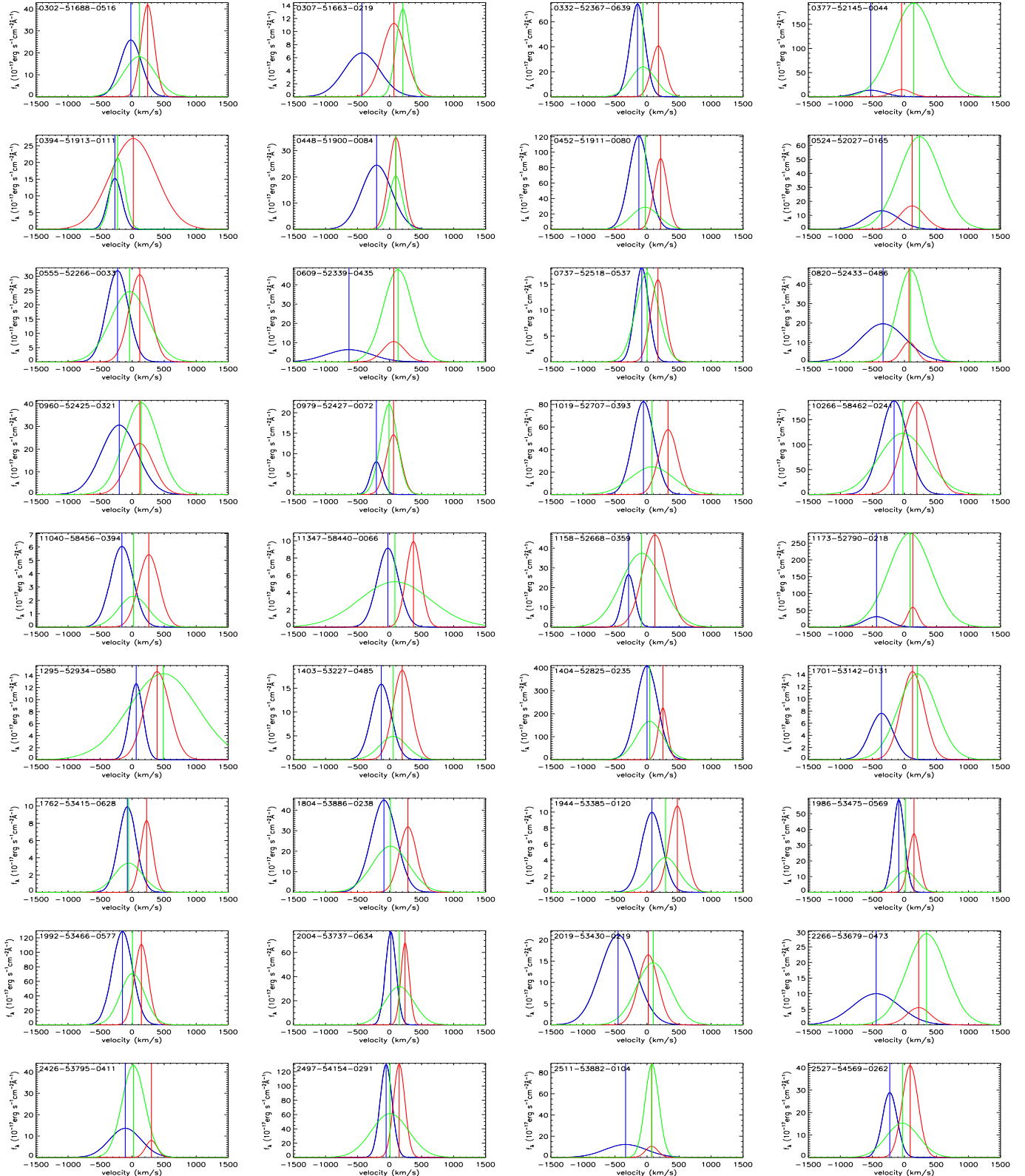


Figure 15. The offsets of [O III] and narrow H α emission lines for the 53 objects with single-peaked narrow H α emission lines in our sample in velocity space. In each panel, the solid blue line represents the determined blue-shifted component of [O III], and the vertical blue line marks the position of the central wavelength of the blue-shifted component of [O III], the solid red line represents the determined red-shifted component of [O III], and the vertical red line marks the position of the central wavelength of the red-shifted component of [O III], the solid green line shows the determined narrow H α component, and the vertical green line marks the position of the central wavelength of the narrow H α .

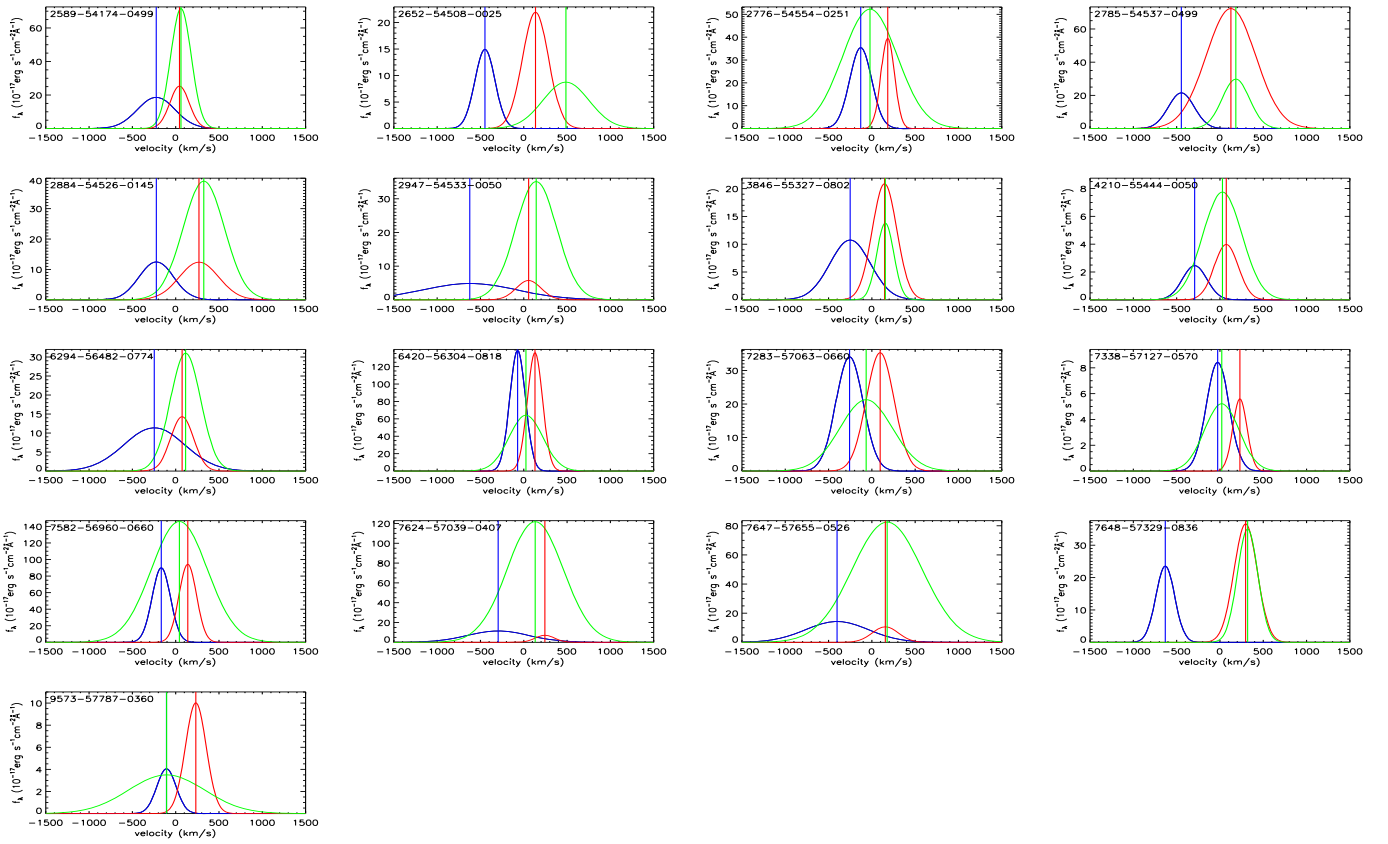


Figure 15. – to be continued

- Comerford, J.M.; Gerke, B.F.; Stern, D., et al., 2012, ApJ, 753, 42
- Comerford, J. M.; Pooley, D.; Barrows, R. S., et al., 2015, ApJ, 806, 219
- Comerford, J.M.; Nevin, R.; Stemo, A., et al., 2018, ApJ, 867, 66
- De Rosa, A.; Vignali, C.; Bogdanović, T., et al., 2019, NewAR, 8601525
- Decarli, R.; Dotti, M.; Mazzucchelli, C., et al., 2014, MNRAS, 445, 1558
- Dotti, M.; Ruszkowski, M., 2010, ApJ, 713, 37
- Dotti, M.; Volonteri, M.; Perego, A., 2010, MNRAS, 402, 682
- Duric, N.; Seaquist, E. R., 1988, ApJ, 326, 574
- Fitzpatrick, E. L., 1999, PASP, 111, 63
- Fu, H.; Myers, A.D.; Djorgovski, S.G., et al, 2011a, ApJ, 733, 103
- Fu, H.; Zhang, Z. Y.; Assef, R. J., et al., 2011b, ApJ, 740, 44
- Fu, H.; Yan, L.; Myers, A.D., et al., 2012, ApJ, 745, 67
- García-Burillo, S., Combes, F., Hunt, L. K., et al., 2003, A&A, 407, 485
- Ge, J. Q., Hu, C., Wang, J. M., et al., 2012, ApJS, 201, 31
- Gerke, B.F.; Newman, J.A.; Lotz, J., et al., 2007, ApJ, 660, 23
- Giarratana, S., Giroletti, M., Spingola, C., et al., 2023, A&A, 670, 35
- Goulding, A.D.; Pardo, K.; Greene, J.E., et al., 2019, ApJ, 879, 21
- Greene, J. E.; Ho, L. C., 2005a, ApJ, 627, 721
- Greene, J. E., Ho, L. C., 2005b, ApJ, 630, 122
- Heckman, T. M., Krolik, J. H., Moran, S. M., et al., 2009, ApJ, 695, 363
- Heckman, T. M., Best, P. N., 2014, ARA&A, 52, 589
- Helfand, D. J., White, R. L., Becker, R. H., 2015, ApJ, 801, 26
- Kauffmann, G.; Heckman, T. M.; Tremonti, C., et al., 2003, MNRAS, 346, 1055
- Kellermann, K. I., Sramek, R., Schmidt, M., et al., 1989, AJ, 98, 1195
- Kim, D. C.; Yoon, I.; Evans, A. S., 2020, ApJ, 904, 23
- Kolmogorov, A. N. 1933, Giornale dell'Istituto Italiano degli Attuari, 4, 83, <http://digitale.bnc.roma.sbn.it/tecadigitale/giornale/CFI0353791/1933/unico>
- Komossa, S., Burwitz, V., Hasinger, G., et al., 2003, ApJ, 582, 15
- Komossa, S., 2006, MmSAI, 77, 733
- Komossa, S., Zhou, H.; Lu, H., 2008, ApJ, 678, 81
- Komossa, S.; Grupe, D.; Parker, M. L., 2021, MNRAS, 504, 5575
- Kormendy, J., Richstone, D., 1995, ARA&A, 33, 581
- Kormendy, J.; Ho, L. C., 2013, ARA&A, 51, 511
- Kovacevic, J.; Popovic, L. C.; Dimitrijevic, M. S., 2010, ApJS, 189, 15
- Kynoch, D., Mitchell, J. A. J., Ward, M. J., et al., 2023, MNRAS, 520, 2781
- Laine, S., Dey, L., Valtonen, M., 2020, ApJ, 894, 1
- Li, W., Nair, P., Irwin, J., et al., 2023, ApJ, 944, 168
- Liu, X.; Shen, Y.; Strauss, M.A., 2010a, ApJ, 708, 427
- Liu, X.; Greene, J. E.; Shen, Y., et al., 2010b, ApJL, 715, 30
- Liu, X., Shen, Y., Strauss, M. A., et al., 2011, ApJ, 737, 101
- Liu, X., Civano, F., Shen, Y., 2013, ApJ, 762, 110
- Lyke, B. W., Higley, A. N., McLane, J. N., et al., 2020, ApJS, 250, 8
- Lyu, Y.; Liu, X., 2016, MNRAS, 463, 24
- Magorrian, J., Tremaine, S., Richstone, D., 1998, AJ, 115, 2285
- Makridakis, S., Wheelwright, S. C., Hyndman, R. J., 1997 Forecasting: Methods and Applications (John Wiley & Sons)
- Marconi, A., & Hunt, L. K. 2003, ApJ, 589, L21
- Markwardt, C. B., 2009, ASPC, 411, 251
- Maschmann, D., Melchior, A.L., Mamon, G.A., et al., 2020, A&A, 641, 171
- Maschmann, D., Halle, A., Melchior, A., et al., 2023, A&A, 670, 46
- May, D.; Steiner, J. E., 2017, MNRAS, 469, 994
- Mayer, L.; Bonoli, S., 2019, RPPh, 82, 6901
- McGurk, R. C., Max, C. E., Rosario, D. J., 2011, ApJ, 738, 2
- McGurk, R. C.; Max, C. E.; Medling, A. M., et al., 2015, ApJ, 811, 14
- Mejía-Restrepo, J. E.; Trakhtenbrot, B.; Koss, M. J., 2022, ApJS, 261, 5
- Merritt, D.; Milosavljević, M., 2005, LRR, 8, 8
- Müller-Sánchez, F.; Comerford, J.M.; Nevin, R., et al, 2015, ApJ, 813, 103
- Nevin, R.; Comerford, J.; Müller-Sánchez, F., et al, 2016, ApJ, 832, 67
- Rafiee, A., & Hall, P. B. 2011, ApJS, 194, 42
- Páris, I., Petitjean, P., Aubourg, E., 2018, A&A, 613, 51
- Perna, M., Arribas, S., Marshall, M., et al., 2023, A&A, 679, 89
- Peterson, B. M., Ferrarese, L., Gilbert, K. M., et al. 2004, ApJ, 613, 682
- Rosario, D.J.; McGurk, R.C.; Max, C.E., et al, 2011, ApJ, 739, 44
- Ross, N. P., Myers, A. D., Sheldon, E. S., 2012, ApJS, 199, 3
- Rubinur, K.; Das, M.; Kharb, P., 2019, MNRAS, 484, 4933
- Salviander, S., Shields, G. A., Gebhardt, K., 2007, ApJ, 662, 131
- Saturni, F. G.; Vietri, G.; Piconcelli, E., et al., 2021, A&A, 654, 154
- Severgnini, P.; Braito, V.; Cicone, C., et al, 2021, A&A, 646, 153
- Shen, Y.; Liu, X.; Greene, J.E., et al, 2011a, ApJ, 735, 48
- Shen, Y.; Richards, G. T.; Strauss, M., et al., 2011b, ApJS, 194, 45
- Shen, Y., Hwang, H., Zakamska, N., et al., 2019, ApJ, 885, 4
- Shi, Z.X.; Luo, A.L; Comte, G., et al, 2014, RAA, 14, 1234
- Shields, G. A.; Bonning, E. W.; Salviander, S., 2009, ApJ, 696, 1367
- Sikora, M., Stawarz, L., Lasota, J., 2007, ApJ, 658, 815
- Silk, J.; Rees, M. J.; 1998, A&A, 331, 1
- Springel, V.; Di Matteo, T.; Hernquist, L., 2005, MNRAS, 361, 776
- Smirnov, N. 1948, Ann. Math. Stat., 19, 27
- Smith, K.L.; Shields, G.A.; Bonning, E.W., et al, 2010, ApJ, 716, 866
- Smith, K.L.; Shields, G.A.; Salviander, S., et al, 2012, ApJ, 752, 63
- S, 1908, the probable error of a mean, Biometrika 4, 1-24
- Villforth, C.; Hamann, F., 2015, AJ, 149, 92

- Wang, J.M.; Chen, Y.M.; Hu, C., et al, 2009, ApJ, 705, 76
- Wang, M.X.; Luo, A.L.; Song, Y.H., et al, 2019, MNRAS, 482, 1889
- White, R. L., Becker, R. H., Helfand, D. J., et al., 1997, ApJ, 475, 479
- Whittle, M.; Wilson, A. S., 2004, AJ, 127, 606
- Wizinowich, P. L.; Le Mignant, D.; Bouchez, A. H., et al., 2006, PASP, 118, 297
- Woo, J.H.; Cho, H.; Husemann, B., et al, 2014, MNRAS, 437, 32
- Xu, D.W.; Komossa, S., 2009, ApJ, 705, 20
- Yao, S.; Yang, X.L.; Gu, M.F., et al, 2021, MNRAS, 508, 1305
- Zhang, X. G., 2014, MNRAS, 438, 557
- Zhang, X.G.; Feng, L.L., 2016, MNRAS, 457, 3878
- Zhang, X. G., 2021a, ApJ, 919, 13
- Zhang, X. G., 2021b, ApJ, 909, 16
- Zhang, Y. W., Huang, Y.; Bai, J. M., et al., 2021, AJ, 162, 289
- Zhang, X. G.,Zheng, Q., 2023, MNRAS, 520, 6190
- Zhang, X. G., 2024a, ApJ, 961, 82
- Zhang, X. G., 2024b, MNRAS, 529, 41
- Zheng, Q., Liu, S., Zhang, X. G.,et al., 2023, ApJ, 944, 4
- Zheng, Q., Zhang, X. G., Yuan, Q. R., et al., 2024, MNRAS, tmpL, 32
- Zhou, H.Y.; Wang, T.G.; Zhang, X.G., et al, 2004, ApJ, 604, 33
- Zuo, P.; Ho, L. C.; Wang, J., et al., 2022, ApJ, 929, 15

B. FULL DATA TABLES OF THE 62 TYPE 1 AGNS

In this appendix, the tables of the 62 type 1 AGNs are provided. Information of the 62 AGNs in the final sample is listed in Table 6 including Plate-Mjd-Fiberid, RA, DEC, redshift, photometric magnitude in r -band, S/N. The parameters of broad H α and H β emission lines are listed in Table 7. The features of [N II] and narrow H α emission lines are listed in Table 8. Meanwhile, the modeled parameters of double-peaked [O III] and the results of F-test are shown in Table 9.

Table 6. sample information

Plate-Mjd-Fiberid (1)	RA (2)	DEC (3)	z (4)	magr (5)	S/N (6)	FIRST (7)	R (8)	Reference (9)
0302-51688-0516	212.51527	0.21395	0.14	18.4±0.01	15.19	0	0	-
0307-51663-0219	219.25504	-1.07168	0.29	19.03±0.08	11.15	0	0	-
0332-52367-0639	184.03066	-2.23828	0.1	17.28±0.01	29.36	0	0	(1),(2)
0377-52145-0044	340.12026	-1.11381	0.13	17.25±0.02	27.98	0	0	-
0394-51913-0111	13.6107	-0.339	0.17	19.03±0.01	25.54	10.53	237.98	-
0448-51900-0084	133.73845	54.80571	0.26	18.2±0.02	15.73	1.31	11.78	-
0452-51911-0080	145.43677	57.85658	0.16	17.97±0.01	15.12	0	0	(1),(2),(6),(7)
0524-52027-0165	196.07083	2.09365	0.23	17.33±0.02	25.71	0	0	-
0555-52266-0033	144.88269	54.81924	0.29	18.31±0.01	15.56	0	0	-
0609-52339-0435	221.95334	62.74577	0.23	18.49±0.02	11.75	0	0	(1),(2),(8)
0737-52518-0537	336.40999	14.11419	0.13	18.53±0.02	14.02	-	-	-
0820-52433-0486	254.17532	36.51368	0.14	18.29±0.01	18.07	1.46	9.92	-
0907-52373-0295	162.24439	54.8897	0.15	18.31±0.02	12.98	0	0	-
0960-52425-0321	203.1581	59.51494	0.17	17.29±0.02	38.4	0.92	2.51	-
0979-52427-0072	260.33538	26.61622	0.16	18.69±0.03	13.88	0	0	-
1019-52707-0393	183.67094	55.60951	0.13	17.84±0.01	19.79	0	0	-
10266-58462-0241	166.76885	32.10834	0.24	17.34±0.02	29.54	2.82	15.28	-
1048-52736-0416	222.79193	49.13712	0.16	18.22±0.02	14.91	0.89	5.59	(2),(3),(4)
11040-58456-0394	10.42232	16.77411	0.17	18.9±0.02	19.87	-	-	-
11347-58440-0066	145.77147	28.09336	0.27	17.52±0.01	29.17	0	0	-
1158-52668-0359	206.56623	58.00226	0.16	17.45±0.03	23.48	1.71	5.95	-
1173-52790-0218	248.4095	37.22063	0.12	17.65±0.08	23.13	0	0	-
1295-52934-0580	123.92722	6.58972	0.24	17.98±0.02	21.7	0	0	(1),(2),(4),(7),(8),(9),(10)
1403-53227-0485	237.96583	33.76054	0.23	19.07±0.02	10.33	0	0	-
1404-52825-0235	238.57263	32.64384	0.05	16.37±0.01	37.92	2.52	2.86	-
1679-53149-0532	233.13253	42.06188	0.21	18.17±0.02	24.65	0	0	(2),(4),(6),(8),(10),(11),(12)
1701-53142-0131	206.62306	10.87407	0.29	18.25±0.01	15.91	0	0	-
1762-53415-0628	179.15898	15.08357	0.19	18.70±0.03	10.28	0	0	-
1804-53886-0238	205.86365	8.37615	0.24	18.07±0.01	19.15	1.73	8.90	-
1944-53385-0120	145.77147	28.09337	0.27	17.52±0.01	27.9	0	0	-
1986-53475-0569	187.3235	40.7632	0.17	18.31±0.02	14.14	0	0	-
1992-53466-0577	187.95448	39.09172	0.07	17.36±0.01	26.24	2.31	8.21	-
2004-53737-0634	184.24977	32.51835	0.13	17.69±0.02	28.34	0	0	(1),(2)
2019-53430-0219	159.46766	31.41677	0.15	18.26±0.01	18.68	2.15	121.32	-
2022-53827-0553	192.05762	36.40656	0.21	18.34±0.02	16	2.93	22.04	(1),(2),(4),(7),(8),(9)
2266-53679-0473	120.00024	15.39059	0.27	19.09±0.02	11.55	6.73	112.92	-
2365-53739-0359	153.17171	21.93225	0.11	18.49±0.02	21.93	0	0	(1),(2),(4),(6),(10)
2426-53795-0411	128.66508	12.04501	0.25	18.53±0.01	15.42	2.18	18.66	-

Continued on next page

Continued

Plate-Mjd-Fiberid (1)	RA (2)	DEC (3)	z (4)	mag _r (5)	S/N (6)	FIRST (7)	R (8)	Reference (9)
2497-54154-0291	169.94838	23.59432	0.15	17.88±0.01	21.38	0	0	-
2511-53882-0104	177.51928	21.04227	0.13	17.79±0.02	20.81	0	0	-
2527-54569-0262	242.61423	13.13523	0.23	18.79±0.45	11.36	0	0	(1),(2),(6),(7),(10),(11),(12)
2589-54174-0499	155.07937	17.61328	0.18	17.99±0.02	21.11	0.85	5.18	-
2652-54508-0025	202.23245	21.59238	0.13	17.88±0.03	16.57	5.92	459.61	(2)
2776-54554-0251	220.27352	18.08556	0.11	17.69±0.02	22.86	0	0	(1),(2),(4)
2785-54537-0499	212.67293	22.5603	0.17	17.5±0.02	22.67	3.68	17.61	(8)
2791-54556-0005	225.61673	19.04929	0.26	18.83±0.02	11.29	0	0	-
2884-54526-0145	244.96114	50.09315	0.28	19.24±0.01	12.1	2.34	65.56	-
2947-54533-0050	221.95334	62.74576	0.23	18.49±0.01	15.94	0	0	-
3830-55574-0154	153.35855	-0.02679	0.26	18.51±0.02	16.62	1.69	24.49	-
3846-55327-0802	184.80754	0.6809	0.29	18.4±0.02	21.5	0	0	-
4210-55444-0050	351.07114	-0.94571	0.2	19.67±0.02	12.33	0	0	(2)
6294-56482-0774	342.15175	28.88209	0.17	18.59±0.01	20.24	-	-	-
6420-56304-0818	169.94837	23.59432	0.15	17.88±0.01	25.37	0	0	-
7283-57063-0660	144.88269	54.81922	0.29	18.31±0.01	17.47	0	0	-
7338-57127-0570	212.3154	53.45606	0.26	19.24±0.03	13.65	0	0	-
7582-56960-0660	336.32782	21.03436	0.14	18.17±0.03	29.16	-	-	-
7624-57039-0407	15.00198	19.19814	0.3	17.2±0.02	36.62	-	-	-
7647-57655-0526	333.09655	29.51795	0.25	17.25±0.01	42.61	-	-	-
7648-57329-0836	336.11891	26.23979	0.21	17.95±0.02	33.06	-	-	(5)
7723-58430-0620-	16.67971	34.04106	0.18	18.5±0.01	21.95	-	-	-
7875-56980-0296	17.96095	-2.54367	0.23	19.45±0.03	13.54	-	-	-
9573-57787-0360	155.7179	17.99481	0.25	18.39±0.02	19.27	0	0	-

Notes. Column 1: Plate, MJD, Fiberid of spectroscopic observation; Column 2: RA; Column 3: DEC; Column 4: Redshift of spectroscopic observation; Column 5: Apparent psf magnitude in r band; Column 6: Median signal-to-noise over all good pixels; Column 7: Integrated FIRST radio flux(mJy); Column 8: Radio-loudness; Column 9: Reference:(1) Zhang & Feng (2016); (2) Smith et al. (2010); (3) Ge et al. (2012); (4) Smith et al. (2012); (5) Zheng et al. (2024); (6) Fu et al. (2012); (7) Comerford et al. (2018); (8) Kim et al. (2020b); (9) Comerford et al. (2012); (10) McGurk et al. (2015); (11) Rosario et al. (2011); (12) Fu et al. (2011a).

Table 7. Line parameters of broad H α and broad H β

Plate-Mjd-Fiberid (1)	$\lambda_{H\alpha}$ (2)	FWHM _{Hα} (3)	$F_{H\alpha}$ (4)	$\lambda_{H\beta}$ (5)	FWHM _{Hβ} (6)	$F_{H\beta}$ (7)	mass (8)
0302-51688-0516	6559.7 ± 5.0	72.3 ± 5.7	918.7 ± 116.2	4850.9 ± 3.1	35.9 ± 5.4	96.4 ± 17.7	7.81 ± 0.10
0307-51663-0219	6569.2 ± 0.6	47.7 ± 5.0	881.3 ± 55.5	4864.9 ± 0.8	43.7 ± 2.6	188.6 ± 9.3	7.50 ± 0.11
0332-52367-0639	6565.3 ± 1.6	99.4 ± 3.9	3770.8 ± 226.9	4870.1 ± 2.1	102.5 ± 5.9	768.8 ± 50.6	7.98 ± 0.05
0377-52145-0044	6546.1 ± 0.5	73.3 ± 5.4	4751.0 ± 153.0	4859.9 ± 1.6	50.8 ± 2.8	1154.8 ± 66.7	7.80 ± 0.07
0394-51913-0111	6566.3 ± 1.7	35.2 ± 4.0	1141.8 ± 94.9	4863.3 ± 1.9	23.2 ± 4.6	46.0 ± 10.5	7.77 ± 0.12
0448-51900-0084	6567.9 ± 0.3	40.8 ± 4.5	1700.1 ± 58.8	4865.3 ± 1.7	35.2 ± 5.9	544.7 ± 28.4	7.28 ± 0.11
0452-51911-0080	6555.0 ± 0.8	48.8 ± 2.1	2213.3 ± 33.9	4857.4 ± 4.3	130.1 ± 12.4	369.4 ± 31.6	7.59 ± 0.04
0524-52027-0165	6557.9 ± 0.6	48.8 ± 3.0	2387.4 ± 110.1	4857.4 ± 4.3	29.3 ± 12.4	369.4 ± 31.6	7.79 ± 0.07
0555-52266-0033	6566.7 ± 0.7	113.3 ± 1.3	2854.9 ± 66.8	4869.4 ± 16.5	87.2 ± 33.1	824.1 ± 64.6	8.44 ± 0.02

Continued on next page

Continued

Plate-Mjd-Fiberid (1)	$\lambda_{H\alpha}$ (2)	FWHM $H\alpha$ (3)	$F_{H\alpha}$ (4)	$\lambda_{H\beta}$ (5)	FWHM $H\beta$ (6)	$F_{H\beta}$ (7)	mass (8)
0609-52339-0435	6561.2 ± 0.8	76.5 ± 1.7	1051.7 ± 30.6	4878.4 ± 15.8	51.3 ± 35.6	541.9 ± 72.0	7.69 ± 0.03
0737-52518-0537	6570.6 ± 0.4	54.7 ± 2.2	2010.9 ± 86.9	4867.0 ± 1.9	38.9 ± 5.6	140.4 ± 14.8	7.91 ± 0.05
0820-52433-0486	6572.7 ± 0.6	63.3 ± 4.1	1329.8 ± 68.0	4868.8 ± 4.0	49.7 ± 8.6	230.1 ± 24.8	7.57 ± 0.07
0907-52373-0295	6566.7 ± 2.4	114.1 ± 7.2	711.2 ± 41.2	4863.9 ± 6.1	58.1 ± 18.0	70.8 ± 20.6	8.22 ± 0.07
0960-52425-0321	6579.6 ± 1.3	165.0 ± 3.3	2965.6 ± 61.9	4891.4 ± 5.4	152.1 ± 13.6	935.0 ± 85.6	8.45 ± 0.02
0979-52427-0072	6572.0 ± 0.6	73.0 ± 1.8	951.6 ± 21.8	4881.0 ± 20.8	56.6 ± 9.0	316.5 ± 51.1	7.39 ± 0.03
1019-52707-0393	6569.2 ± 0.9	70.9 ± 2.7	3344.8 ± 162.9	4873.4 ± 1.7	65.5 ± 14.5	998.0 ± 54.6	7.63 ± 0.05
10266-58462-0241	6562.1 ± 0.7	177.7 ± 1.3	10224.7 ± 103.2	4866.9 ± 1.0	131.5 ± 3.1	2926.8 ± 37.4	9.05 ± 0.01
1048-52736-0416	6578.3 ± 3.9	134.4 ± 15.5	1845.5 ± 601.7	4877.2 ± 6.5	85.2 ± 11.9	193.7 ± 32.5	8.60 ± 0.18
11040-58456-0394	6537.1 ± 0.9	145.5 ± 4.3	2581.4 ± 56.0	4842.7 ± 2.7	147.1 ± 11.2	416.7 ± 33.6	8.60 ± 0.03
11347-58440-0066	6562.6 ± 1.6	149.4 ± 2.0	4960.8 ± 128.5	4879.0 ± 2.2	123.5 ± 11.4	1363.5 ± 62.7	8.79 ± 0.02
1158-52668-0359	6572.5 ± 0.7	80.5 ± 6.1	2545.9 ± 150.8	4867.5 ± 2.2	62.0 ± 4.5	559.9 ± 35.1	7.91 ± 0.08
1173-52790-0218	6571.8 ± 0.3	60.5 ± 4.0	4879.2 ± 209.3	4865.2 ± 0.2	26.1 ± 3.7	2227.0 ± 91.9	7.46 ± 0.07
1295-52934-0580	6553.9 ± 0.6	50.2 ± 2.0	3060.3 ± 41.2	4873.3 ± 0.5	73.5 ± 1.7	1257.6 ± 58.4	7.57 ± 0.04
1403-53227-0485	6551.6 ± 1.1	196.0 ± 3.5	2225.8 ± 35.6	4882.9 ± 3.4	181.6 ± 16.2	458.1 ± 62.6	8.89 ± 0.02
1404-52825-0235	6568.2 ± 0.3	91.9 ± 1.7	19953.0 ± 477.4	4871.1 ± 1.2	78.2 ± 10.3	4664.7 ± 117.1	7.88 ± 0.02
1679-53149-0532	6580.2 ± 3.1	180.5 ± 3.4	3620.9 ± 103.1	4884.3 ± 5.8	198.9 ± 7.9	1382.9 ± 114.3	8.68 ± 0.02
1701-53142-0131	6569.3 ± 1.0	104.9 ± 2.4	2001.1 ± 47.6	4868.8 ± 2.9	92.0 ± 6.5	720.8 ± 41.8	8.23 ± 0.03
1762-53415-0628	6570.1 ± 0.7	86.6 ± 4.7	1410.4 ± 37.1	4860.7 ± 6.7	78.6 ± 8.4	277.3 ± 49.8	7.98 ± 0.05
1804-53886-0238	6575.7 ± 0.9	132.9 ± 2.2	4639.5 ± 72.1	4886.0 ± 3.0	134.5 ± 11.8	1180.5 ± 71.9	8.65 ± 0.02
1944-53385-0120	6568.4 ± 0.5	141.3 ± 1.1	6090.6 ± 62.3	4878.6 ± 1.4	114.5 ± 15.6	1810.7 ± 92.6	8.75 ± 0.01
1986-53475-0569	6560.3 ± 0.6	105.9 ± 1.5	1698.9 ± 24.4	4860.6 ± 2.0	99.9 ± 5.3	477.1 ± 22.3	7.97 ± 0.02
1992-53466-0577	6568.2 ± 0.3	94.9 ± 2.5	5756.7 ± 130.5	4867.9 ± 1.7	77.0 ± 3.9	621.5 ± 33.5	8.13 ± 0.03
2004-53737-0634	6567.0 ± 0.5	68.0 ± 2.3	3821.1 ± 141.8	4868.2 ± 0.8	55.8 ± 17.7	1068.2 ± 35.8	7.61 ± 0.04
2019-53430-0219	6571.4 ± 0.6	50.4 ± 3.3	490.7 ± 60.2	4861.0 ± 2.1	23.0 ± 0.8	47.9 ± 15.1	7.45 ± 0.09
2022-53827-0553	6562.2 ± 0.8	161.7 ± 2.3	2317.6 ± 32.2	4865.2 ± 3.8	144.1 ± 9.2	631.4 ± 36.5	8.54 ± 0.02
2266-53679-0473	6562.0 ± 0.7	63.0 ± 3.0	1405.6 ± 61.5	4860.0 ± 1.1	42.8 ± 2.3	188.9 ± 11.0	8.05 ± 0.05
2365-53739-0359	6565.7 ± 2.2	98.3 ± 3.1	3187.0 ± 269.9	4865.1 ± 2.8	77.3 ± 3.7	842.2 ± 66.7	7.86 ± 0.05
2426-53795-0411	6567.1 ± 1.3	32.5 ± 4.6	797.0 ± 103.1	4868.2 ± 9.0	33.5 ± 18.9	197.1 ± 26.4	6.99 ± 0.16
2497-54154-0291	6572.3 ± 0.4	112.4 ± 1.3	3998.7 ± 40.3	4867.5 ± 1.2	77.4 ± 5.1	1634.4 ± 39.1	8.09 ± 0.01
2511-53882-0104	6566.4 ± 0.5	44.5 ± 2.6	1283.4 ± 88.0	4861.8 ± 3.4	39.7 ± 6.3	251.2 ± 47.9	7.16 ± 0.07
2527-54569-0262	6570.3 ± 1.1	139.2 ± 3.6	1087.4 ± 25.7	4880.2 ± 8.5	109.9 ± 13.2	230.5 ± 38.1	8.40 ± 0.03
2589-54174-0499	6569.2 ± 0.2	38.5 ± 0.6	1121.0 ± 20.4	4868.7 ± 5.0	28.1 ± 14.3	345.2 ± 27.4	6.95 ± 0.02
2652-54508-0025	6566.2 ± 1.2	45.9 ± 1.5	616.5 ± 48.1	4861.7 ± 1.7	23.2 ± 0.2	63.9 ± 9.7	7.31 ± 0.05
2776-54554-0251	6565.7 ± 0.4	74.2 ± 3.8	5179.5 ± 180.4	4867.3 ± 4.9	61.0 ± 9.3	929.5 ± 123.1	7.88 ± 0.05
2785-54537-0499	6567.2 ± 0.2	65.1 ± 1.3	7659.4 ± 137.9	4866.1 ± 0.8	54.7 ± 2.0	1339.9 ± 29.7	8.12 ± 0.02
2791-54556-0005	6574.9 ± 0.4	61.0 ± 1.3	1802.8 ± 33.4	4868.2 ± 0.7	57.5 ± 1.8	533.1 ± 16.3	7.69 ± 0.02
2884-54526-0145	6558.9 ± 1.9	50.8 ± 2.1	477.0 ± 44.8	4858.4 ± 4.9	25.4 ± 0.5	28.5 ± 8.3	7.98 ± 0.06
2947-54533-0050	6560.0 ± 0.7	72.1 ± 1.9	1100.2 ± 117.9	4867.7 ± 3.5	46.0 ± 16.8	467.7 ± 24.4	7.63 ± 0.05
3830-55574-0154	6570.6 ± 0.8	121.2 ± 1.9	2005.1 ± 33.7	4867.3 ± 1.1	63.4 ± 4.2	195.5 ± 13.1	8.82 ± 0.02
3846-55327-0802	6564.4 ± 0.1	30.1 ± 1.0	1438.7 ± 31.3	4862.1 ± 0.9	46.9 ± 2.6	249.3 ± 10.0	7.30 ± 0.04
4210-55444-0050	6564.3 ± 0.4	36.0 ± 2.6	432.1 ± 23.9	4861.6 ± 1.6	31.5 ± 5.3	34.6 ± 5.3	7.32 ± 0.08
6294-56482-0774	6573.6 ± 0.2	41.6 ± 1.1	1208.1 ± 20.5	4860.8 ± 0.9	23.9 ± 0.7	81.8 ± 7.7	7.68 ± 0.03
6420-56304-0818	6565.6 ± 1.1	64.2 ± 1.3	5869.2 ± 129.5	4865.4 ± 0.6	82.2 ± 2.0	1486.1 ± 22.1	7.79 ± 0.02
7283-57063-0660	6559.2 ± 0.2	91.5 ± 0.8	2982.2 ± 19.2	4863.9 ± 0.6	89.9 ± 1.7	476.4 ± 8.0	8.52 ± 0.01

Continued on next page

Continued

Plate-Mjd-Fiberid (1)	$\lambda_{H\alpha}$ (2)	FWHM $H\alpha$ (3)	$F_{H\alpha}$ (4)	$\lambda_{H\beta}$ (5)	FWHM $H\beta$ (6)	$F_{H\beta}$ (7)	mass (8)
7338-57127-0570	6573.2 ± 2.5	168.0 ± 4.0	576.1 ± 22.8	4864.0 ± 1.5	146.6 ± 16.4	147.0 ± 15.6	8.39 ± 0.03
7582-56960-0660	6552.8 ± 0.2	59.8 ± 2.7	2439.2 ± 51.2	4861.1 ± 0.8	43.0 ± 1.7	668.8 ± 22.8	7.46 ± 0.04
7624-57039-0407	6564.6 ± 0.2	60.6 ± 1.4	5090.0 ± 73.0	4862.9 ± 0.4	35.2 ± 1.2	1541.9 ± 42.7	8.01 ± 0.02
7647-57655-0526	6565.8 ± 0.2	65.6 ± 2.0	6017.8 ± 106.8	4863.1 ± 0.3	58.3 ± 0.8	1481.5 ± 17.8	8.10 ± 0.03
7648-57329-0836	6565.6 ± 0.2	59.7 ± 0.5	4232.3 ± 33.8	4880.3 ± 0.8	74.5 ± 11.6	1189.5 ± 51.4	7.78 ± 0.01
7723-58430-0620	6575.0 ± 0.8	189.7 ± 1.9	3324.5 ± 41.4	4867.1 ± 2.3	229.8 ± 6.3	796.5 ± 27.1	8.74 ± 0.01
7875-56980-0296	6573.4 ± 1.1	56.3 ± 2.8	1475.9 ± 26.9	4873.6 ± 6.7	59.5 ± 13.9	285.9 ± 27.7	7.71 ± 0.05
9573-57787-0360	6560.7 ± 2.0	105.1 ± 8.3	2049.2 ± 103.7	4862.6 ± 1.3	111.4 ± 3.4	480.1 ± 14.1	8.31 ± 0.08

Notes. Column 1: Plate, MJD, Fiberid of spectroscopic observation; Column 2 and Column 3: the central wavelength (the first moment) of broad H α in units of Å and corresponding FWHM of broad H α in units of Å determined through the line profiles described by two Gaussian functions, respectively; Column 4: corresponding flux of broad H α in units of 10^{-17} erg/s/cm 2 determined by the line flux described by two Gaussian functions; Column 5 and Column 6: the central wavelength (the first moment) of broad H β in units of Å and corresponding FWHM of broad H β in units of Å determined through the line profiles described by two Gaussian functions, respectively; Column 7: corresponding flux of broad H β in units of 10^{-17} erg/s/cm 2 determined by the line flux described by two Gaussian functions; Column 8: the virial black hole mass log(M_{BH}/M $_{\odot}$).

Table 8. Features of narrow H α and [N II] emission lines

Plate-Mjd-Fiberid (1)	$\lambda_{H\alpha}$ (2)	$\sigma_{H\alpha}$ (3)	$F_{H\alpha}$ (4)	$\lambda_{[N\text{ II}]}$ (5)	$\sigma_{[N\text{ II}]}$ (6)	$F_{[N\text{ II}]}$ (7)
0302-51688-0516	6567.1 ± 0.2	5.3 ± 0.3	244.6 ± 23.8	6587.0 ± 0.2	4.7 ± 0.3	135.8 ± 14.0
0307-51663-0219	6569.1 ± 0.2	2.3 ± 0.2	77.4 ± 7.8	6589.3 ± 0.3	3.2 ± 0.3	70.7 ± 8.8
0332-52367-0639	6563.3 ± 0.2	4.3 ± 0.3	254.6 ± 25.8	6583.9 ± 0.2	4.2 ± 0.3	289.2 ± 26.5
0377-52145-0044	6567.8 ± 0.1	7.2 ± 0.1	3502.1 ± 55.5	6586.1 ± 0.3	4.9 ± 0.3	409.6 ± 38.0
0394-51913-0111	6559.6 ± 0.1	2.3 ± 0.1	125.7 ± 5.2	6585.2 ± 0.1	6.9 ± 0.2	471.1 ± 28.3
0448-51900-0084	6566.7 ± 0.1	2.2 ± 0.2	113.0 ± 8.9	6587.7 ± 0.2	4.2 ± 0.2	235.3 ± 13.6
0452-51911-0080	6564.0 ± 0.2	4.7 ± 0.2	339.4 ± 13.2	6585.0 ± 0.2	4.6 ± 0.2	281.5 ± 11.4
0524-52027-0165	6569.8 ± 0.1	7.1 ± 0.2	1176.8 ± 54.4	6592.7 ± 0.2	2.9 ± 0.2	107.9 ± 11.4
0555-52266-0033	6563.8 ± 0.4	6.5 ± 0.2	401.0 ± 19.8	6580.6 ± 1.0	8.0 ± 0.9	190.7 ± 35.3
0609-52339-0435	6567.5 ± 0.1	5.0 ± 0.1	600.3 ± 13.8	6586.4 ± 0.1	4.7 ± 0.2	276.5 ± 12.0
0737-52518-0537	6564.7 ± 0.2	3.9 ± 0.3	166.7 ± 17.3	6585.9 ± 0.6	4.1 ± 0.8	49.7 ± 13.3
0820-52433-0486	6566.7 ± 0.1	4.5 ± 0.1	534.4 ± 19.5	6587.0 ± 0.1	4.5 ± 0.1	322.0 ± 15.2
0907-52373-0295	6564.1 ± 0.6	7.9 ± 0.6	224.8 ± 21.2	6585.3 ± 0.3	6.0 ± 0.3	249.2 ± 15.3
0960-52425-0321	6567.7 ± 0.1	5.9 ± 0.1	595.4 ± 10.9	6587.1 ± 0.1	4.7 ± 0.1	591.4 ± 11.5
0979-52427-0072	6564.4 ± 0.1	2.9 ± 0.1	161.2 ± 6.7	6585.7 ± 0.2	3.3 ± 0.3	86.1 ± 8.1
1019-52707-0393	6566.3 ± 0.4	7.3 ± 0.4	451.7 ± 34.0	6587.5 ± 0.2	5.5 ± 0.2	472.1 ± 26.5
10266-58462-0241	6564.1 ± 0.1	8.3 ± 0.1	2546.3 ± 46.3	6578.7 ± 0.4	10.8 ± 0.3	1215.2 ± 50.2
1048-52736-0416	6564.2 ± 0.1	4.5 ± 0.1	540.1 ± 12.4	6584.0 ± 0.2	4.5 ± 0.3	226.7 ± 14.7
11040-58456-0394	6565.0 ± 1.0	5.0 ± 1.2	29.2 ± 8.6	6585.6 ± 1.5	3.0 ± 1.8	8.0 ± 5.6
11347-58440-0066	6566.4 ± 1.2	12.2 ± 1.9	160.2 ± 34.4	6584.9 ± 0.4	2.1 ± 0.5	23.4 ± 6.7
1158-52668-0359	6562.8 ± 0.4	7.0 ± 0.3	659.3 ± 42.7	6584.0 ± 0.3	7.7 ± 0.3	1052.7 ± 58.6
1173-52790-0218	6566.5 ± 0.1	7.4 ± 0.1	5152.0 ± 89.1	6583.9 ± 0.6	5.6 ± 0.5	397.6 ± 70.1
1295-52934-0580	6575.2 ± 0.9	11.8 ± 0.6	422.0 ± 18.2	6597.6 ± 0.6	11.8 ± 0.4	427.5 ± 18.4
1403-53227-0485	6565.9 ± 0.5	4.6 ± 0.5	56.8 ± 5.9	6585.9 ± 0.6	3.0 ± 0.6	22.0 ± 4.4

Continued on next page

Continued

Plate-Mjd-Fiberid (1)	$\lambda_{H\alpha}$ (2)	$\sigma_{H\alpha}$ (3)	$F_{H\alpha}$ (4)	$\lambda_{[N\text{ II}]}$ (5)	$\sigma_{[N\text{ II}]}$ (6)	$F_{[N\text{ II}]}$ (7)
1404-52825-0235	6565.5±0.1	4.5±0.1	1888.1±59.4	6586.4±0.1	4.5±0.1	1420.8±52.6
1679-53149-0532	6563.9±0.1	6.0±0.1	731.9±14.9	6584.0±0.3	6.8±0.3	373.0±16.4
1701-53142-0131	6569.0±0.4	6.5±0.4	230.1±16.4	6589.5±0.3	4.0±0.4	110.7±11.0
1762-53415-0628	6563.4±0.9	4.8±1.1	40.7±11.3	6587.0±0.8	4.1±1.0	30.4±9.2
1804-53886-0238	6564.9±0.3	6.2±0.3	350.7±16.5	6585.6±0.3	5.1±0.3	243.4±15.3
1944-53385-0120	6570.9±1.3	4.5±1.2	49.5±15.1	6590.2±1.2	8.0±1.5	127.2±25.8
1986-53475-0569	6564.9±0.2	3.6±0.2	121.9±7.5	6585.1±0.3	3.3±0.3	65.4±6.7
1992-53466-0577	6564.7±0.1	4.1±0.1	733.1±20.6	6585.3±0.2	4.6±0.2	372.0±20.5
2004-53737-0634	6567.9±0.2	4.9±0.2	390.3±23.8	6587.2±0.2	3.5±0.2	173.8±13.9
2019-53430-0219	6566.8±0.3	5.8±0.5	212.1±36.7	6586.1±0.2	4.5±0.3	169.7±21.1
2022-53827-0553	6565.1±0.2	4.4±0.2	166.1±8.9	6585.6±0.3	4.7±0.3	122.8±8.2
2266-53679-0473	6572.2±0.3	6.8±0.2	500.7±19.6	6587.4±0.2	5.3±0.2	347.9±21.8
2365-53739-0359	6564.4±0.1	4.3±0.2	475.9±30.0	6584.5±0.2	4.4±0.2	297.1±26.4
2426-53795-0411	6565.1±0.1	3.9±0.2	421.6±32.9	6585.1±0.1	3.5±0.2	252.1±25.1
2497-54154-0291	6564.8±0.2	6.4±0.1	981.6±20.2	6582.5±0.4	6.3±0.3	337.5±23.2
2511-53882-0104	6566.3±0.1	2.4±0.1	520.7±12.7	6586.7±0.1	2.7±0.1	241.0±10.3
2527-54569-0262	6563.9±0.2	5.6±0.2	213.9±8.2	6583.6±0.2	4.9±0.2	158.9±8.0
2589-54174-0499	6565.9±0.1	2.6±0.1	465.6±11.1	6586.3±0.1	2.5±0.1	274.1±7.8
2652-54508-0025	6575.3±0.9	5.8±0.8	127.9±29.5	6589.0±0.6	5.3±0.5	142.7±23.2
2776-54554-0251	6564.1±0.2	6.9±0.2	906.5±53.7	6584.5±0.2	6.2±0.3	669.3±46.4
2785-54537-0499	6568.6±0.2	3.5±0.3	258.0±24.8	6590.6±0.2	3.9±0.2	300.8±20.6
2791-54556-0005	6563.5±0.3	7.3±0.4	323.8±26.0	6588.3±0.3	1.5±0.4	19.6±4.9
2884-54526-0145	6571.7±0.1	5.2±0.1	510.7±19.6	6591.4±0.1	4.9±0.2	324.7±17.8
2947-54533-0050	6567.7±0.1	5.2±0.1	458.3±10.8	6586.1±0.1	5.0±0.2	209.5±8.8
3830-55574-0154	6565.1±0.2	8.1±0.2	722.4±17.6	6585.9±0.2	8.5±0.2	698.4±21.7
3846-55327-0802	6568.0±0.1	2.1±0.1	74.1±6.0	6588.8±0.3	3.9±0.2	69.9±5.4
4210-55444-0050	6565.2±0.2	4.9±0.3	95.9±11.2	6588.1±0.4	2.7±0.4	17.9±3.2
6294-56482-0774	6567.1±0.1	3.8±0.1	296.9±10.5	6587.9±0.1	3.2±0.1	180.5±5.6
6420-56304-0818	6565.1±0.1	4.3±0.1	687.4±32.0	6583.1±0.3	5.4±0.5	160.3±32.1
7283-57063-0660	6563.2±0.2	6.6±0.2	352.3±9.8	6582.5±0.6	5.1±0.6	57.2±8.8
7338-57127-0570	6565.1±0.2	4.4±0.2	57.4±3.1	6586.9±0.3	3.7±0.3	39.4±3.6
7582-56960-0660	6565.5±0.1	7.1±0.1	2581.0±27.1	6584.7±0.1	4.6±0.1	402.9±14.7
7624-57039-0407	6567.5±0.1	7.1±0.1	2164.5±38.1	6589.7±0.4	3.1±0.5	47.7±9.1
7647-57655-0526	6568.5±0.1	8.9±0.2	1834.1±59.6	6588.5±0.3	4.1±0.3	222.0±20.4
7648-57329-0836	6571.6±0.1	2.6±0.1	226.3±11.4	6591.2±0.1	3.3±0.2	189.1±10.1
7723-58430-0620-	6565.6±0.1	7.2±0.1	809.6±11.8	6585.8±0.2	6.4±0.1	437.2±11.8
7875-56980-0296	6561.9±0.1	1.5±0.1	22.9±2.2	6590.1±0.3	1.6±0.3	9.4±1.7
9573-57787-0360	6562.3±1.0	9.6±0.8	84.6±10.0	6587.9±1.1	3.7±1.2	14.8±5.2

Notes. Column 1: Plate, MJD, Fiberid of spectroscopic observation; Column 2: the central wavelength of narrow H α in units of Å; Column 3: corresponding second moment of narrow H α in units of Å; Column 4: corresponding flux of narrow H α in units of $10^{-17}\text{erg/s/cm}^2$; Column 5: the central wavelength of narrow [N II] in units of Å; Column 6: corresponding second moment of [N II] in units of Å; Column 7: corresponding flux of [N II] in units of $10^{-17}\text{erg/s/cm}^2$.

Table 9. Features of [O III]

Plate-Mjd-Fiberid (1)	λ_b (2)	σ_b (3)	F_b (4)	λ_r (5)	σ_r (6)	F_r (7)	F-test (8)	V_b (9)	V_r (10)
0302-51688-0516	5007.9 ± 0.5	2.8 ± 0.3	178.9 ± 29.6	5012.3 ± 0.1	1.7 ± 0.1	180.2 ± 28.4	5	173.2 ± 41.9	435.6 ± 19.4
0307-51663-0219	5001.0 ± 0.9	4.6 ± 0.6	78.2 ± 13.8	5009.4 ± 0.3	3.1 ± 0.2	87.3 ± 13.0	3	-	-
0332-52367-0639	5005.8 ± 0.1	1.9 ± 0.1	360.5 ± 16.0	5011.2 ± 0.2	1.8 ± 0.1	181.2 ± 15.6	5	112.5 ± 16.2	214.0 ± 19.8
0377-52145-0044	4999.5 ± 0.7	3.6 ± 0.7	121.2 ± 24.1	5007.5 ± 0.5	2.5 ± 0.4	94.5 ± 21.8	3	-	-
0394-51913-0111	5003.7 ± 0.1	1.8 ± 0.1	69.5 ± 7.0	5008.5 ± 0.2	6.0 ± 0.2	409.3 ± 32.4	5	203.3 ± 15.6	83.8 ± 22.1
0448-51900-0084	5004.9 ± 0.6	3.9 ± 0.5	239.1 ± 47.1	5009.9 ± 0.1	1.9 ± 0.1	164.6 ± 30.4	5	-	-
0452-51911-0080	5006.1 ± 0.1	2.6 ± 0.1	776.8 ± 19.7	5011.8 ± 0.1	1.7 ± 0.1	390.0 ± 17.9	5	21.2 ± 20.4	319.3 ± 20.0
0524-52027-0165	5002.4 ± 1.2	4.3 ± 0.7	143.0 ± 36.4	5010.3 ± 0.6	3.3 ± 0.3	136.9 ± 35.8	3	-	-
0555-52266-0033	5004.4 ± 0.3	2.8 ± 0.2	227.4 ± 25.4	5010.2 ± 0.3	2.8 ± 0.2	210.8 ± 26.4	5	-	-
0609-52339-0435	4997.7 ± 0.7	5.8 ± 1.0	93.6 ± 18.8	5009.3 ± 0.2	2.8 ± 0.2	74.7 ± 9.7	5	387.7 ± 69.4	311.2 ± 40.5
0737-52518-0537	5006.9 ± 0.4	1.8 ± 0.2	82.2 ± 16.1	5011.1 ± 0.4	1.9 ± 0.3	74.4 ± 16.2	5	39.8 ± 29.9	292.5 ± 34.3
0820-52433-0486	5002.7 ± 0.5	5.9 ± 0.4	290.6 ± 35.6	5009.4 ± 0.2	2.0 ± 0.3	50.3 ± 14.1	5	144.4 ± 42.7	260.2 ± 25.2
0907-52373-0295	5005.0 ± 0.2	2.2 ± 0.3	114.4 ± 21.5	5011.0 ± 0.1	1.8 ± 0.1	129.2 ± 14.9	5	124.3 ± 24.4	237.4 ± 20.7
0960-52425-0321	5004.9 ± 0.2	4.7 ± 0.3	362.2 ± 21.0	5010.2 ± 0.3	3.5 ± 0.2	198.3 ± 15.4	3	52.2 ± 21.7	373.0 ± 29.3
0979-52427-0072	5004.8 ± 0.4	1.5 ± 0.3	30.3 ± 9.2	5009.3 ± 0.3	1.9 ± 0.2	71.3 ± 9.8	3	83.9 ± 43.1	184.1 ± 35.3
1019-52707-0393	5007.3 ± 0.2	2.8 ± 0.1	572.3 ± 37.0	5013.7 ± 0.2	2.4 ± 0.2	347.6 ± 35.3	5	172.2 ± 22.5	556.4 ± 25.2
10266-58462-0241	5005.6 ± 0.5	3.5 ± 0.2	1671.7 ± 299.4	5011.5 ± 0.5	3.6 ± 0.2	1677.9 ± 295.7	3	-	-
1048-52736-0416	5005.4 ± 0.2	1.7 ± 0.1	160.9 ± 18.7	5009.8 ± 0.3	1.8 ± 0.2	137.9 ± 18.8	5	99.9 ± 32.8	166.2 ± 36.6
11040-58456-0394	5005.6 ± 0.6	2.9 ± 0.5	44.4 ± 9.1	5012.6 ± 0.7	2.7 ± 0.5	36.4 ± 8.9	4	45.4 ± 52.5	375.2 ± 53.2
11347-58440-0066	5007.8 ± 0.3	2.8 ± 0.4	63.9 ± 16.4	5014.5 ± 0.2	1.9 ± 0.2	48.2 ± 8.7	5	-	-
1158-52668-0359	5003.4 ± 0.2	1.6 ± 0.2	106.6 ± 27.2	5010.3 ± 0.2	3.2 ± 0.3	374.9 ± 74.0	5	269.9 ± 24.0	141.4 ± 24.6
1173-52790-0218	5001.0 ± 0.2	3.2 ± 0.3	245.8 ± 55.9	5010.4 ± 0.1	1.4 ± 0.1	204.1 ± 14.1	5	-	-
1295-52934-0580	5009.3 ± 0.2	1.8 ± 0.2	55.8 ± 13.6	5014.7 ± 0.4	3.3 ± 0.4	119.9 ± 23.4	5	-	-
1403-53227-0485	5006.1 ± 0.5	2.5 ± 0.3	101.3 ± 17.5	5011.5 ± 0.4	2.4 ± 0.2	112.5 ± 17.5	5	119.3 ± 62.8	445.8 ± 56.9
1404-52825-0235	5008.2 ± 0.1	2.8 ± 0.1	2859.1 ± 87.9	5012.4 ± 0.1	1.2 ± 0.1	669.4 ± 69.7	5	150.0 ± 12.1	397.2 ± 9.6
1679-53149-0532	5005.0 ± 0.1	2.1 ± 0.1	608.2 ± 17.6	5010.8 ± 0.1	2.0 ± 0.0	563.2 ± 17.2	5	-	-
1701-53142-0131	5002.2 ± 0.5	3.0 ± 0.4	57.8 ± 9.1	5010.4 ± 0.3	3.0 ± 0.2	108.9 ± 9.2	3	-	-
1762-53415-0628	5007.0 ± 0.4	2.3 ± 0.4	57.8 ± 10.1	5012.0 ± 0.3	1.6 ± 0.3	33.3 ± 8.6	4	10.8 ± 45.5	311.3 ± 42.0
1804-53886-0238	5006.8 ± 0.3	3.3 ± 0.3	372.5 ± 53.3	5013.0 ± 0.3	2.2 ± 0.2	179.1 ± 32.1	5	-	-
1944-53385-0120	5009.5 ± 0.4	2.7 ± 0.5	66.9 ± 22.2	5016.2 ± 0.3	2.1 ± 0.3	57.9 ± 15.2	5	-	-
1986-53475-0569	5006.8 ± 0.1	1.5 ± 0.1	216.3 ± 11.3	5010.7 ± 0.1	1.4 ± 0.1	130.2 ± 10.9	5	38.1 ± 22.5	274.9 ± 25.0
1992-53466-0577	5005.7 ± 0.1	2.6 ± 0.1	849.6 ± 43.2	5010.7 ± 0.1	1.8 ± 0.1	501.1 ± 38.4	5	98.8 ± 17.4	197.0 ± 15.0
2004-53737-0634	5008.6 ± 0.0	1.4 ± 0.0	265.2 ± 8.1	5012.3 ± 0.0	1.1 ± 0.0	184.8 ± 7.4	5	248.8 ± 11.6	471.4 ± 11.5
2019-53430-0219	5000.7 ± 0.5	4.7 ± 0.3	247.4 ± 20.5	5008.6 ± 0.2	2.6 ± 0.2	105.6 ± 19.2	5	303.5 ± 38.6	168.0 ± 26.2
2022-53827-0553	5005.0 ± 0.0	2.0 ± 0.0	253.8 ± 5.9	5011.3 ± 0.0	1.8 ± 0.0	211.1 ± 5.3	5	143.2 ± 25.9	235.8 ± 25.9
2266-53679-0473	5000.9 ± 0.4	6.1 ± 0.4	153.1 ± 17.0	5012.0 ± 0.3	3.1 ± 0.3	42.5 ± 8.0	5	48.2 ± 48.9	616.2 ± 46.3
2365-53739-0359	5005.8 ± 0.1	1.7 ± 0.0	585.6 ± 22.6	5010.1 ± 0.1	1.8 ± 0.0	600.0 ± 23.1	5	97.3 ± 17.4	158.9 ± 17.4
2426-53795-0411	5006.5 ± 0.3	4.1 ± 0.4	141.5 ± 18.6	5013.3 ± 0.2	1.5 ± 0.2	29.7 ± 7.0	5	43.9 ± 37.1	451.7 ± 30.3
2497-54154-0291	5007.3 ± 0.1	1.6 ± 0.1	510.7 ± 39.0	5010.7 ± 0.1	1.5 ± 0.1	490.3 ± 38.9	5	87.0 ± 22.8	290.9 ± 22.4
2511-53882-0104	5002.7 ± 0.7	5.4 ± 0.6	164.9 ± 21.1	5009.5 ± 0.2	1.6 ± 0.3	42.9 ± 13.1	5	152.5 ± 55.0	254.6 ± 26.5
2527-54569-0262	5004.4 ± 0.1	1.9 ± 0.1	138.9 ± 9.4	5009.7 ± 0.1	2.1 ± 0.1	214.0 ± 9.8	5	202.4 ± 32.9	116.2 ± 31.0
2589-54174-0499	5004.5 ± 0.9	3.6 ± 0.5	169.6 ± 37.6	5009.0 ± 0.1	1.9 ± 0.2	119.0 ± 34.9	5	-	-
2652-54508-0025	5000.8 ± 0.2	1.9 ± 0.3	72.5 ± 15.0	5010.5 ± 0.2	2.5 ± 0.2	138.0 ± 23.3	5	547.3 ± 24.4	36.3 ± 23.4
2776-54554-0251	5006.1 ± 0.2	2.1 ± 0.2	188.0 ± 24.0	5011.3 ± 0.1	1.3 ± 0.1	128.9 ± 13.8	5	29.3 ± 21.0	282.7 ± 18.4

Continued on next page

Continued

Plate-Mjd-Fiberid (1)	λ_b (2)	σ_b (3)	F_b (4)	λ_r (5)	σ_r (6)	F_r (7)	F-test (8)	V_b (9)	V_r (10)
2785-54537-0499	5000.8 ± 0.2	2.5 ± 0.3	134.4 ± 36.5	5010.4 ± 0.2	4.8 ± 0.2	866.5 ± 95.9	5	-	-
2791-54556-0005	5004.9 ± 0.1	2.2 ± 0.1	171.3 ± 13.6	5010.3 ± 0.2	1.8 ± 0.2	69.3 ± 10.4	5	-	-
2884-54526-0145	5004.5 ± 0.4	3.3 ± 0.2	103.2 ± 12.9	5012.7 ± 0.4	3.8 ± 0.3	117.8 ± 14.1	5	292.6 ± 38.7	784.9 ± 42.3
2947-54533-0050	4997.8 ± 0.7	9.1 ± 0.7	110.1 ± 9.8	5009.2 ± 0.2	2.4 ± 0.2	34.2 ± 4.6	3	-	-
3830-55574-0154	5007.5 ± 0.2	5.4 ± 0.2	1118.8 ± 70.9	5013.7 ± 0.1	2.1 ± 0.1	305.2 ± 27.7	5	-	-
3846-55327-0802	5004.1 ± 0.5	3.9 ± 0.4	105.3 ± 13.5	5010.7 ± 0.1	2.4 ± 0.1	123.6 ± 11.2	5	41.4 ± 41.2	438.5 ± 20.3
4210-55444-0050	5003.4 ± 0.7	2.4 ± 0.5	14.5 ± 4.1	5009.5 ± 0.4	2.3 ± 0.3	23.1 ± 4.1	3	50.9 ± 58.2	314.2 ± 41.9
6294-56482-0774	5004.1 ± 0.6	5.9 ± 0.6	167.6 ± 51.6	5009.5 ± 0.1	2.2 ± 0.1	79.0 ± 9.9	5	6.7 ± 49.8	314.9 ± 19.6
6420-56304-0818	5007.1 ± 0.1	1.5 ± 0.0	523.5 ± 28.4	5010.4 ± 0.1	1.5 ± 0.0	496.0 ± 28.9	5	-	-
7283-57063-0660	5003.9 ± 0.2	2.6 ± 0.1	223.4 ± 15.9	5009.8 ± 0.2	2.7 ± 0.1	237.2 ± 16.5	5	-	-
7338-57127-0570	5007.8 ± 0.4	2.2 ± 0.3	46.4 ± 6.9	5012.1 ± 0.3	1.4 ± 0.2	19.1 ± 5.8	4	137.4 ± 39.1	394.1 ± 34.8
7582-56960-0660	5005.5 ± 0.0	1.8 ± 0.0	397.8 ± 9.2	5010.6 ± 0.0	1.7 ± 0.0	397.8 ± 8.2	5	-	-
7624-57039-0407	5003.3 ± 0.4	5.9 ± 0.4	170.5 ± 10.9	5012.3 ± 0.2	1.8 ± 0.3	32.9 ± 6.7	5	-	-
7647-57655-0526	5001.5 ± 0.6	6.1 ± 0.6	217.5 ± 23.1	5010.8 ± 0.2	2.5 ± 0.3	67.0 ± 16.5	5	-	-
7648-57329-0836	4997.7 ± 0.1	1.8 ± 0.1	106.8 ± 7.1	5013.2 ± 0.1	2.2 ± 0.1	205.5 ± 10.2	5	-	-
7723-58430-0620	5007.6 ± 0.1	3.7 ± 0.1	1182.4 ± 38.9	5013.8 ± 0.1	2.2 ± 0.0	533.0 ± 31.2	5	-	-
7875-56980-0296	5006.2 ± 0.1	1.8 ± 0.0	140.8 ± 3.8	5011.5 ± 0.0	1.6 ± 0.0	130.1 ± 3.6	5	14.6 ± 20.6	333.0 ± 20.5
9573-57787-0360	5006.5 ± 0.4	1.9 ± 0.4	18.8 ± 4.5	5012.1 ± 0.2	2.0 ± 0.2	50.4 ± 4.8	3	-	-

Notes. Column 1: Plate, MJD, Fiberid of spectroscopic observation; Column 2: the central wavelength of blue-shifted component of [O III] in units of Å; Column 3: corresponding second moment of blue-shifted component of [O III] in units of Å; Column 4: corresponding flux of blue-shifted component of [O III] in units of 10^{-17} erg/s/cm²; Column 5: the central wavelength of red-shifted component of [O III] in units of Å; Column 6: corresponding second moment of red-shifted component of [O III] in units of Å; Column 7: corresponding flux of red-shifted component of [O III] in units of 10^{-17} erg/s/cm²; Column 8: the confidence level (σ) of F-test; Column 9 and Column 10: the velocity offset of blue-shifted component and red-shifted component of [O III] determined by shifted velocity from SSP method in units of km/s, respectively, and ‘-’ represents an object with no obvious absorption line.